

NON-INVASIVE CHOROIDAL IMAGING AND RETINAL, CHOROIDAL AND
OPTIC NERVE HEAD OXYGEN SATURATION CALCULATIONS USING A
MULTISPECTRAL SNAPSHOT IMAGING SYSTEM WITH VISIBLE AND NEAR
INFRARED WAVELENGTHS

AN ABSTRACT

SUBMITTED ON THE FIFTH DAY OF MAY 2013

TO THE DEPARTMENT OF NEUROSCIENCE

IN PARTIAL FULFILLMENT OF THE REQUIREMENTS

OF THE SCHOOL OF SCIENCE AND ENGINEERING

OF TULANE UNIVERSITY

FOR THE DEGREE

OF

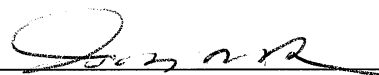
MASTER OF NEUROSCIENCE

BY



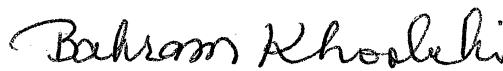
KIM ALEXIS FIRN

APPROVED:



JEFFREY TASKER, Ph.D.

Director



BAHRAM KHOUBEHI, Ph.D.



BETH WEE, Ph.D.

ABSTRACT

PURPOSE. To image the fundus non-invasively at two different penetration depths using a multispectral imaging system. Monochromatic images at visible spectrum wavelengths and near-infrared wavelengths were qualitatively assessed for choroidal visibility. These images were used calculate oxygen saturation in retinal tissue, optic nerve head tissue, vein, and choroidal tissue in healthy controls and glaucoma patients.

METHODS. A fundus camera-based multispectral snapshot oximeter imaged the fundus of healthy subjects and patients with varying ophthalmological pathology. The images of healthy controls and glaucoma patients were analyzed to determine oxygen saturation in the optic nerve head cup and rim, superficial and deep vein, macula and choroidal tissue.

RESULTS. Visible: Average oxygen saturation for the ONH cup was 65 ± 6 percent for healthy controls and 61 ± 10 percent for glaucoma patients. For the ONH rim, it was 67 ± 3 percent for healthy controls and 64 ± 17 percent for glaucoma patients. For the vein, it was 67 ± 15 percent for healthy controls and 56 ± 22 percent for glaucoma patients. For the macula, it was 87 ± 10 percent for healthy controls and 93 ± 1 percent for glaucoma patients. NIR: The average oxygen saturation for the vein was 66 ± 20 percent for healthy controls, 58 ± 0.4 percent for glaucoma suspects and 54 ± 17 percent for glaucoma patients. For the choroidal tissue below the macula, it was 99 ± 5 percent in healthy controls and 81 ± 8 percent in glaucoma patients.

CONCLUSIONS. Choroidal visibility is enhanced in near infrared monochromatic images from visible spectrum monochromatic images. Oxygen saturation results were lower in glaucoma patients for all anatomical areas analyzed except the avascular macula.

NON-INVASIVE CHOROIDAL IMAGING AND RETINAL, CHOROIDAL AND
OPTIC NERVE HEAD OXYGEN SATURATION CALCULATIONS USING A
MULTISPECTRAL SNAPSHOT IMAGING SYSTEM WITH VISIBLE AND NEAR
INFRARED WAVELENGTHS

A THESIS

SUBMITTED ON THE FIFTH DAY OF MAY 2013

TO THE DEPARTMENT OF NEUROSCIENCE

IN PARTIAL FULFILLMENT OF THE REQUIREMENTS

OF THE SCHOOL OF SCIENCE AND ENGINEERING

OF TULANE UNIVERSITY

FOR THE DEGREE


OF

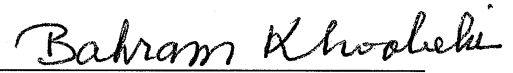
MASTER OF NEUROSCIENCE

BY


KIM ALEXIS FIRN

APPROVED:


JEFFREY TASKER, Ph.D.
Director


BAHRAM KHOUBEHI, Ph.D.


BETH WEE, Ph.D.

ACKNOWLEDGMENTS

I would like to acknowledge and thank Dr. Bahram Khoobehi for being my mentor for the last five years and for being so helpful in the laboratory. It has truly been a pleasure to work with him and I hope to continue to do so in the future. I would like to thank Dr. Jeffrey Tasker and Dr. Beth Wee for helping me with suggestions for this thesis and for being amazing professors. I would like to acknowledge the Louisiana State University Health Sciences Center for providing a laboratory for our work and the Louisiana State University Eye Center on St. Charles Avenue for providing the clinic where we obtained data. Specifically, I would like to thank Dr. Yen Ngo and Dr. Philip Kikuchi for guiding me and referring patients. Lastly, I would like to thank Tulane University for providing coursework that complemented my research in the learning process.

TABLE OF CONTENTS

ACKNOWLEDGMENTS	ii
LIST OF FIGURES	iv-v
LIST OF TABLES	vi
INTRODUCTION	1
METHODS	15
RESULTS	19
Visualization	19
Oxygen Saturation	19
DISCUSSION	22
APPENDICES	27
LIST OF REFERENCES	50

LIST OF FIGURES

- Figure 1: Spectral curves for Hb and HbO₂
- Figure 2: Image depicting intensity point selections from within and outside a vessel
- Figure 3: Monochromatic images of the optic nerve head taken at 570 nm and 600 nm
- Figure 4: Monochromatic images of the retina taken at 570 nm and 600 nm
- Figure 5: Monochromatic fundus image at 570 nm with an oxygen saturation overlay
- Figure 6: Schematic of hyperspectral imaging acquisition
- Figure 7: Schematic of the hyperspectral imaging design
- Figure 8: Hyperspectral image cube
- Figure 9: Graphical depiction of Khoobehi et al.'s saturation algorithm
- Figure 10: Schematic of the fundus camera Zeiss FF450 IR
- Figure 11: Schematic of the relay sub-system and reimaging lenses
- Figure 12: Evidence of reproducibility
- Figure 13: Expanded view of the HbO₂ and Hb curves
- Figure 14: Division of trapezoids in the oxygen saturation index algorithm
- Figure 15: Image key identifying analyzed areas around the optic nerve head
- Figure 16: Penetration depth in millimeters
- Figure 17: Images from a healthy control using visible wavelengths

Figure 18: Images from a healthy control using NIR wavelengths

Figure 19: Images from a wet AMD patient using visible wavelengths

Figure 20: Images from the wet AMD patient using NIR wavelengths

Figure 21: Image of a glaucoma patient exhibiting bulging of the ONH cup

LIST OF TABLES

Table 1: Oxygen saturation results from the retinal areas shown in Figure 15

Table 2: Demographic data

Table 3: Oxygen saturation results for areas of interest in monochromatic images

Table 4: Differences between saturation of areas of interest and 96 percent saturation

INTRODUCTION

Many diseases of the eye and brain have been successfully diagnosed and monitored using fundus imaging. The eye has been considered a window into the health and functional aspects of the brain. Choroidal tissue is challenging to image because it lies posterior to the retinal pigment epithelium (RPE). Imaging techniques using the visible spectrum of wavelengths, such as traditional fundus imaging, ophthalmoscopy, and fundus fluorescein angiography are limited to imaging the anatomy of the eye anterior the RPE. The RPE absorbs visible light focused onto the retina by the lens, so it also absorbs visible light employed for imaging systems. The lens and the macula lutea absorb shorter wavelength light.¹

Bruch's membrane separates the RPE from the choroid, which provides oxygen and nutrients to the outer retina through its extensive capillary network. The choriocapillaris is closest to Bruch's membrane, and the larger choroidal vessels lie deeper. The vascularization is mostly limited to the choroid because vessels in the retina would interfere with image formation. Retinal vascularization surrounds the macula, a highly pigmented yellow oval in the center of the retina. The fovea is the area in the center of the macula responsible for high visual acuity, so it is especially important for this area to be avascular. The central retina, which forms a six millimeter circle around the fovea, is much thicker than the peripheral retina due to the high density of cones and close packing of these photoreceptors for high visual acuity. However, the center of the

fovea is the thinnest part of the retina due to lateral displacement of amacrine, horizontal, bipolar and ganglion cells. This allows light to directly hit the photoreceptors in this area and limits light scattering by more superficial cell layers. The foveal cone cells are compacted into their most efficient packing density, a hexagonal mosaic. The periphery of the fovea, called the parafovea or foveal rim, is the thickest area of the retina because the cells laterally displaced from the center of the fovea are packed in this area.² The fovea can be seen in fundus images as an avascular area in the center of the macula, temporal to the optic nerve head (ONH). Retinal ganglion cell axons join together in the ONH and project to the lateral geniculate nucleus, where visual information is relayed before being sent to the visual cortex. Retinal topography is maintained in the ONH.

The choroid has three vascular layers: outer arteries and veins, medial arterioles and venules and an inner capillary bed, called the choriocapillaris.³ Choroidal arteries arise from ciliary arteries and Zinn's circle, the area around the optic disc. The posterior ciliary artery makes a semi-circular turn before reaching Bruch's membrane. Arteries that pierce the sclera near the optic nerve fan out to form the three choroidal vascular layers. This has been visualized with a corrosion cast of a cut face of the human choroid.⁴ Oxygen and nutrients from the choroid are delivered to the RPE and are essential to visual function. The RPE uses this support to transport ions, water and nutrients from the subretinal space to the blood, take up nutrients from the blood and deliver them to the photoreceptors, exchange isomers of retinal with photoreceptors in the visual cycle, stabilize ion composition in the subretinal space to maintain photoreceptor excitability, engulf and digest photoreceptor outer segments and secrete growth and

immunosuppressive factors. The RPE integrity is also vital because it helps make up the retina-blood barrier.

The fundus of the eye can be seen with an ophthalmoscope or fundus camera if the pupil is fully dilated. Fundus Fluorescein Angiography (FFA) uses interference bandpass filters to only allow light of certain wavelengths to pass. The exciter filter lets light in the 465 nm to 490 nm range pass to the eye to excite the fluorescein dye. The barrier filter lets the emission light in the range of 520 nm to 530 nm pass back to the detector. This technique has the advantage of dye tracing to track circulatory filling. Additionally, hyperfluorescence can indicate leaking defects, such as capillary leakage and neovascularization, pooling defects, staining, transmission defects or abnormal vasculature, and hypofluorescence can indicate blocking defect or filling defect, such as capillary blockage.⁵ Hyperfluorescence signal has been used to indicate choroidal neovascularization (CNV). However, use of fluorescein dye comes with the risk of severe adverse effects.⁶ The use of light in the visible range mostly restricts this technique to use for visualization anterior to the RPE. Indocyanine Green Angiography (ICGA) employs NIR light. This technique can therefore visualize the choroid, but involves indocyanine green (ICG) dye injection and time for the dye to reach the eye.

Non-invasive, quick imaging of the choroid would be a valuable tool in a variety of other pathological conditions, as well. Gross anatomical changes may become apparent with visualization. Further, monochromatic images of the fundus can be used to calculate oxygen saturation in structures of interest. Choroidal imaging has the potential to aid in differentiation between occult and classic CNV and image areas of CNV beneath blood, exudate or pigment epithelium detachment, as can be done with ICGA.⁷

Monitoring of CNV in age-related macular degeneration (AMD) patients also would be valuable for predicting onset of retinal angiomatous proliferation. Punctate inner choroidopathy and serpiginous choroidopathy may be diagnosed more quickly or better monitored with enhanced visualization of these pathologies.

Diabetic choroidopathy (DC) is much less well studied than diabetic retinopathy (DR). This may be due to the lack of non-invasive choroidal imaging to monitor gross anatomical pathologies in DC. Hua et al.⁸ have documented pathoanatomy of DC in prediagnosed DR patients and has produced angiographic and optical evidence for DC using ICGA and Optical Coherence Tomography (OCT). OCT is a method producing cross-sectional images as opposed to the surface imaging methods discussed thus far. The toxic effects of hyperglycemia extend to the choroid, causing a variety of pathological signs.

Lutty et al.⁹ have observed polymorphonuclear leukocytes at sites of endothelial capillary vascular dysfunction in the diabetic choroid. Saker et al.¹⁰ have shown high glucose conditions to significantly increase the permeability of choroidal endothelial cells monolayers. Oxygen saturation analysis of choroidal monochromatic images in these conditions would be valuable to correlate pathology with fluctuations in oxygen levels for future use as a biomarker indicating disease state and appropriate treatment course. Choroidal hyperpermeability also leads to central serous chorioretinopathy and oxygen level fluctuations in this case may be strongly predictive of this condition.

In the case of serous retinal pigment epithelium detachment (PED), ICGA is necessary to identify feeder and drainer vessels in the choroid. CNV is supported by release of vascular endothelial growth factor from the RPE. When treated with anti-

VEGF drugs, about 75 percent of serous PED patients have residual retinal fluid after three to five doses, and 36 percent still have residual fluid after a year of treatment.¹¹ ICGA-assisted identification of choroidal vessels responsible for this fluid build up is used for directed photodynamic therapy to resolve persistent cases of serous retinal PED. However, according to Healio Ophthalmology, about 85 percent of serous PED patients have associated neovascular lesions, such as polypoidal choroidal vasculopathy and arterialized vascular complex. Choroidal visualization in these cases would be valuable and choroidal oxygen saturation levels would provide an additional diagnostic marker for such pathologies.

Submacular choroidal thickness previously has been shown to change in retinitis pigmentosa using OCT.¹² This is possibly indicative of further pathophysiological changes. In fact, Langham has shown relative choroidal ischemia to be associated with visual loss and pigment cell degeneration in retinitis pigmentosa.¹³ Cataract surgery also has been linked to changes in choroidal thickness¹¹ and choroidal effusion.¹⁴ Interestingly, choroidal thickness also has been shown to increase during a migraine attack as compared to baseline, and Dadaci et al.¹⁵ have suggested this may implicate a link between migraines and glaucoma.

Bad cardiovascular health has been known to compromise vision, and there are documented cases of hypertensive choroidopathy. There are also visual abnormalities associated with Alzheimer's disease (AD), which are thought to be due to more than simply cortical defects. The retina already has been suggested to be a window into the health of the brain, and the source of the earliest biomarkers for AD.¹⁶ Retinal ganglion cell degeneration has been shown in glaucoma and AD alike. Morphological and

functional alterations of microglial and neuronal activities of the retina may be present in preclinical AD. Intracellular amyloid beta has been shown to alter the tight junctions between RPE cells in 5XFAD mice.¹⁷ There also have been microvascular network changes in AD patient retinas documented, even when controlling for cerebrovascular disease.¹⁸ More research will likely identify a similar correlational link with the choroid, which may precede retinal defects because the choroid supplies the majority of the blood flow to the retina. Indeed, choroidal thinning in AD already has been shown.¹⁹ Pathological changes have been shown in the choroid and RPE cells of the TgF344 rat model of AD.

In summary, non-invasive, injection-free snapshot imaging of the choroid would be a useful tool aiding the diagnosis and monitoring of many diseases. Oxygen saturation calculations from such images also would help probe the pathophysiology underlying these diseases and provide additional information to clinicians.

Traditional fundus photography has been extended to use for retinal oximetry. Hickam et al.²⁰ then developed the first photographic film method measuring the relative light intensity reflected by oxyhemoglobin (HbO₂) in the retina at discrete wavelengths. Prior to Hickam's work, this intensity was measured from current generated in a photoelectric cell. Hickam et al.²⁰ measured differences in photographic film density of portions of the image corresponding to vessels on the optic disc from a red wavelength and an infrared wavelength to estimate hemoglobin oxygen saturation. Because blood changes color with oxygenation, the spectral signature also changes and can be used to calculate hemoglobin oxygen saturation. Hickam's group's algorithm requires vessels to overlie the optic disc, which acts as a light source. A limitation to this method is that film

grain inhibits the resolution of these images. Principles from this work were later employed to design dual-wavelength methods with high dynamic charged coupled device (CCD) cameras, which boosted sensitivity. Narasimha-Iyer et al.²¹ also discriminated between arteries and veins using a Gaussian-based dual-wavelength method employing wavelengths of 570 nm and 600 nm.

Delori et al.^{22,23} developed the first retinal vessel oximeter utilizing a three wavelength spectro-photometric technique for oxygen saturation measurements in discrete blood vessels. Delori's group employed three wavelengths to overcome the requirement of nonscattering hemolyzed blood in the dual-wavelength technique based on the Lambert-Beer law. This method is able to measure oxygenation of fundus vessels outside the optic disc, unlike Hickam's group's method, because it accounts for light reflected by the RPE and choroid. However, the scanning nature of this system requires 1.4 seconds of retinal immobility.

Riva et al.²⁴ then measured partial pressure of oxygen in optic nerves of pigs using a phosphorescence quenching method. A porphyrin dye injected into venous circulation was excited by a fundus camera-based phosphorometer. This technique is useful, but again, dye injection is not desirable.

Beach et al.²⁵ suggested the use of oxygen-sensitive and oxygen-insensitive wavelengths from the HbO₂ spectral signature for retinal vessel oximetry. Tiedman et al.,²⁶ Beach et al.,²⁵ Schweitzer et al.,²⁷ Hardarson et al.,^{28,29} and Hammer et al.³⁰⁻³² have used this concept to develop retinal oximetry methods measuring optical density, based on Hicham's work with photographic film. These methods employ CCD cameras for advanced sensitivity. The optical density ratio between oxygen-sensitive and oxygen-

insensitive wavelengths has been shown to be proportional to systemic oxygen saturation. These methods are limited to studying oxygenation of retinal vasculature, however.

Khoobehi et al.³⁵ has used a dual-wavelength method to image the retinas of patients with diabetic retinopathy. An oxygen-sensitive wavelength of 570 nm and an oxygen-insensitive wavelength of 600 nm were used, as shown in Figure 1. The light absorption can be described with optical density (OD) according to the equation

$$OD_{\lambda} = \log(I_0/I).$$

Where I_0 is the intensity measured inside a vessel and I is the intensity outside of that vessel. These selections are shown in Figure 2. This value is divided by the tissue intensity outside the vessel to normalize to local conditions.

Optical density is sensitive to oxygen saturation at 600 nm but not at the reference wavelength, 570 nm. The optical densities (absorbance) at each of the two wavelengths were used to calculate a ratio according to the equation

$$ODR = OD_{600 \text{ nm}} / OD_{570 \text{ nm}}$$

The ratio of these optical densities (ODR) is an approximate linear function of hemoglobin oxygen saturation.^{25,34} Oxygen saturation is estimated by the equation

$$SatO_2 = a + kODR,$$

where “a” and “k” are constants that transform the optical densities found experimentally to the ideal 96 percent saturation in arteries and 58 percent in veins.

Saturation values obtained by a calibrated device were matched with optical

density values from controls.^{27,28} Optical density was used by the retinal oximeter to estimate oxygen saturation. Refer to Figures 3 and 4 for images from these two wavelengths. Color-coded oxygen saturation maps can then be produced based on these results as seen in Figure 5.

Khoobehi et al.³⁶ sought to study oxygenation in retinal vasculature as well as retinal tissue. By employing a hyperspectral imaging system (HSI) based on a fundus camera with a scanner, imaging spectrograph and digital camera, Khoobehi's group was able to capture the intensity of reflected light for the complete spectrum of wavelengths in the visible range. Figures 6 and 7 detail image acquisition by this system. Due to the scanning nature of the system, which captures the entire spectrum of wavelengths one spatial line of data at a time, the eye must be immobilized. This method results in a hyperspectral image cube as seen in Figure 8. Involuntary saccadic movements of the eye would blur the image. Therefore, Khoobehi used this system with anesthetized monkeys.

Spectral reflectance curves for HbO₂ and deoxyhemoglobin (Hb) are separated into three regions bound by the isosbestic (oxygen-insensitive) points 522 nm, 548 nm, 569 nm and 586 nm, where there is equal light absorption. Areas trapped between the oxygen-sensitive curve and line segments connecting adjacent isosbestic points are sensitive to oxygen saturation, as shown in Figure 9 by areas a1, a2 and a3. The areas A1, A2 and A3 in Figure 9 are proportional to total reflected light intensity of each area. This is clearly a function of intensity of incident light. Dividing each oxygen saturation-sensitive area between HbO₂ and Hb spectral curves (a1, a2, a3) by the area below it corresponding to total reflected light intensity (A1, A2, A3). The oxygen saturation

component (OSC) is then a combination of oxygen saturation-dependent terms after compensating for total light intensity.

$$\text{OSC} = a_2/A_2 - a_1/A_1 - a_3/A_3$$

The areas in the OSC must also be normalized to blood volume. The area between the hemoglobin spectral curve and the line connecting the isosbestic points at 522 nm and 586 nm is directly proportional to blood volume. This is shown as (b) in Figure 9. The area under this line connecting the isosbestic points 522 nm and 586 nm accounts for total light intensity within this spectral segment. This is (B) in Figure 9. The blood volume component (BVC) normalized to total light intensity is calculated by dividing the blood volume-dependent area by the corresponding total light intensity-dependent area, or b/B. The volume-corrected relative saturation index (RSI) is then:

$$\text{RSI} = \text{OSC} / \text{BVC}$$

In summary, this technique uses HSI to develop an algorithm for oxygen saturation not only in retinal vessels, but also in tissue. This system is valuable in animal research, but the drawback to clinical application is that the scanning nature of the system would require anesthetization.

Khoobehi et al.³⁶ then developed a fundus camera-based multispectral snapshot oximeter to overcome the issue of eye movement. This system employs four isosbestic points and three oxygen-sensitive wavelengths to approximate the whole Hb spectrum. Khoobehi et al. developed an algorithm to approximate the Hb and HbO₂ spectral curves using the intensity at these seven wavelengths. As seen in Figure 9, there are three triangular areas proportional to oxygen saturation, an area proportional to blood volume, and an area proportional to total reflected light intensity. The same calculations from the

HSI system can be made with information from only seven wavelengths. Discrete imaging rules out more precise calculations of the areas trapped between the curves using calculus, but an approximation may be made. With this system, Khoobehi's group was the first to find oxygen saturation in the retinal tissue. Figure 10 shows a schematic of the fundus camera used to produce these monochromatic images. Figure 11 shows a schematic of the lens configuration used to separate the reflected light collected by the camera into seven monochromatic images. Figure 12 shows two color coded oxygen saturation maps of the fundus of the same patient imaged on different days. The images in this figure demonstrate that the results are reproducible. Figure 13 shows an expanded view of the Hb and HbO₂ spectral curves. The area of interest in the visible spectrum from 522 nm to 586 nm encompasses three oxygen saturation-sensitive areas between the HbO₂ and Hb curves.

Figure 14 shows the division of trapezoids in the oxygen saturation index algorithm. The same calculations made from the HSI data can be made from data at seven discrete wavelengths from the multispectral imaging system. Areas a, b, and c are proportional to oxygen saturation and areas 1, 2, 3, 4, 5, and 6 are sensitive to total reflected light intensity. Figure 15 shows areas of the fundus analyzed for oxygen saturation using this multispectral system. Superior, inferior, nasal, and temporal areas of both vein and tissue were measured for each of four distances from the ONH. Those distances were 1) just outside the ONH, 2) 1.5 ONH radii from the ONH edge, 3) 2.5 ONH radii from the ONH edge, and 4) 3.5 ONH radii from the ONH edge. Table 1 shows the oxygen saturation results for these areas. The vein values are calculated by comparing vein intensity to artery intensity, which corresponds to 96 percent saturation.

The tissue values are found to be intermediate between the artery and vein oxygen saturation values.

In this study, the fundus camera-based multispectral snapshot oximeter was used to collect seven monochromatic images in the visible spectrum. Then, the filters in the beam-splitting attachment were changed and the images were collected from seven discrete wavelengths in the NIR region. Figure 16 shows the penetration versus wavelength graph, explaining the hypothesis that the NIR region will penetrate deeper into the fundus to produce monochromatic images of structures at an increased depth. Figure 13 shows an expanded view of the Hb and HbO₂ curves, including both the visible spectrum wavelengths and the NIR region wavelengths of interest. There is only one area between the curves to approximate oxygen saturation information in the longer wavelength, near infrared region.

The images were first analyzed qualitatively for choroidal visibility. A subset of images from healthy controls and glaucoma patients were then analyzed for oxygen saturation calculations from the different wavelength regions, which presumably capture information from different depths within the fundus. Two glaucoma suspects with borderline intraocular pressure (IOP) were included in the NIR region monochromatic vein oxygenation calculation group.

Because glaucoma is a result of elevated IOP, leading to decreased perfusion pressure, autoregulation dysfunction, unstable or decreased ocular blood flow, ischemic insult, ONH damage, and retinal ganglion cell death, the oxygen levels in glaucoma patients are predicted to be lower than in healthy controls. All of these characteristics of glaucoma lead to decreased tissue metabolism and less uptake of oxygen. The choroid

may try to compensate by sending more oxygen to the dying tissue, which appears oxygen deprived. This oxygen, unable to be used by the glaucomatous tissue, may diffuse into the fundus fluid.

Multispectral imaging in the visible spectrum has been employed previously by our lab with variable results. Patients with very lightly pigmented RPEs do not exhibit as much absorption of visible light by the RPE than patients with more heavily pigmented, dark RPEs. Therefore, choroidal visibility is very variable in monochromatic images from the visible spectrum. I hypothesize that wavelengths in the NIR region will penetrate the RPE and the resulting monochromatic images from this region will therefore provide clearer, more consistent visualization of choroidal tissue. Since the NIR region will pass the RPE regardless of pigment variation, monochromatic images at wavelengths in this region will provide a more reliable clinical measure. I also hypothesize that these monochromatic images at NIR wavelengths can be used to calculate oxygen saturation of fundus structures.

Khoobehi et al.³⁶ have shown a more pronounced oxygen saturation decrease in the optic nerve head rim than in the cup in healthy anesthetized monkey retinas sustaining increasing IOP levels. Oxygen saturation levels were calculated from the results of the HSI system. Since these results are from healthy tissue, this study seeks to find the effect in glaucomatous tissue where metabolism is altered.

I hypothesized oxygen saturation in the optic nerve head rim, optic nerve head cup and vein as measured at the depth imaged by monochromatic images in the visible spectrum to be lower in glaucoma patients than in healthy controls. I hypothesized that the oxygen saturation results for the macula at the penetration level of visible

wavelengths will either not exhibit a difference or be higher in glaucoma patients. The oxygen saturation may not change in the macula because my calculations are based on the spectral curves of hemoglobin with and without oxygen bound and the macula lacks hemoglobin. However, due the variation in penetration based on the unique properties of each RPE, the macula oxygen saturation results may account for the most anterior portion of the choroid. The choroid was hypothesized to exhibit a gradient of increasing oxygen saturation from posterior to anterior as it shuttles oxygen to the damaged glaucomatous retinal tissue. Therefore, the macula oxygen saturation calculations may partially account for the higher oxygen content at the anterior portion of the choroid.

I hypothesized oxygen saturation results for the vein at the deeper penetration achieved by the NIR region to be consistent with the more superficial oxygen saturation calculations for the vein because this is a continuous vessel. I hypothesized the choroidal tissue imaged with NIR wavelengths to have the highest oxygen saturation since nearly all the blood entering the eye supplies the choroid.

METHODS

This study was approved by the Institutional Review Board of LSU. It adheres to the tenets of the declaration of Helsinki. All subjects provided informed consent before participation in the study. All subjects went through standard study protocol. After consenting to be in the study, the subjects answered a questionnaire about medical history.

Sixty-four Patients and healthy controls at the LSU Eye Center on St. Charles Avenue already had their pupils dilated for other ophthalmological testing before being imaged by our system. Subjects varied in age from 29 to 87 years and comprised men and women who were white, non-hispanic, Filipino or African American, including one extremely light-skinned African American. Patients' pathology included AMD, ocular hypertension, branch retinal vein occlusion, diabetes, borderline IOP classified as glaucoma suspect, glaucoma or a combination of these pathologies.

All patients and healthy controls were imaged with either the visible spectrum filters or the NIR filters to determine optimal wavelength for choroidal visibility. Next, a subset of these images including those from healthy controls, glaucoma suspects and glaucoma patients were analyzed for oxygen saturation. For the visible spectrum images, Oxygen saturation was calculated for the cup and rim of the ONH, a vein in the optic disc and the macula for healthy controls and glaucoma patients. No glaucoma suspects were imaged with the visible spectrum filters. For the NIR images, oxygen saturation was

calculated for a vein in the optic disc for healthy controls, glaucoma suspects and glaucoma patients and choroidal tissue underlying the macula for healthy controls and glaucoma patients. Demographic data for the groups is seen in Table 2.

For the visible spectrum images, the ONH cup data were obtained by using the maximum intensity values from analyzing an area encompassing the ONH in the ImageJ program. The minimum intensity values from this selection came from the vein within the optic disc with the lowest intensity of reflected light. A small area of the ONH rim excluding any vessels was analyzed, and the mean intensity was used to calculate ONH rim oxygen saturation values. An area encompassing the macula, excluding any vessels was analyzed, and the minimum divided by the maximum intensities of this area were used to calculate oxygen saturation values for the macula. Division by the maximum intensity corrected for any factor that would cause the reflected light to be more intense, such as incident light level or blood volume, which are separately corrected for in the other calculations according to Khoobehi's multispectral oxygen saturation algorithm.

For the NIR images, the minimum divided by the maximum intensities of the area encompassing the optic disc were used to calculate tissue oxygen saturation values. The minimum divided by the maximum intensities from the area encompassing the macula was used to calculate oxygen saturation of the choroidal tissue underlying the macula. The macula was chosen to probe choroidal circulation because this area is avascular in the retina and provides a clear window to the choroid.

A Zeiss FF450 IR fundus camera was employed for this study. A beam splitting attachment was placed on top of the fundus camera to split the reflected light into seven monochromatic images based on the narrowpass filter properties. The fundus camera-

based multispectral snapshot oximeter employs a standard flash from a traditional fundus camera, so the imaging does not pose any risk to the patients. The first phase of the experiment employed the system using filters to produce seven monochromatic images at 522 nm, 542 nm, 548 nm, 560 nm, 569 nm, 577 nm and 586 nm in the visible range of the electromagnetic spectrum. The second phase of the experiment employed the same imaging system but with different filters to produce monochromatic images at 600 nm, 620 nm, 650 nm, 690 nm, 720 nm, 760 nm and 800 nm. The images were analyzed qualitatively for choroidal visualization.

These images were then used to calculate relative oxygen saturation in the groups described previously. Khoobehi's multispectral oxygen saturation algorithm was used to calculate all values for the visible spectrum images. The values were converted to percentages based on taking the intensity of an artery to correspond to 96 percent oxygen saturation. This is the oxygen saturation of a healthy artery *in vivo*.

Only three wavelengths were used to calculate oxygen saturation values for the NIR images because there is only one oxygen-sensitive triangular area in this region. Ideally, two isosbestic points and an oxygen-sensitive point would be used for the calculation. There is, however, only one isosbestic point in the NIR spectrum capable of penetrating through the RPE to the level of the choroid. This isosbestic point is at 800 nm, but this wavelength was unable to yield good images. The second longest wavelength of 760 nm was therefore used in place of 800 nm for the oxygen-sensitive area calculation. Because our system uses narrowpass filters and not more selective bandpass filters, the wavelengths let in by the 760 nm-centered filter are approximately 752 to 768 nm, which is closer to the isosbestic point at 800 nm. The oxygen-sensitive

point selected was at 690 nm, and the less oxygen-sensitive point approximating another isosbestic point was chosen at 620 nm. The calculations for the conversion of this oxygen-sensitive triangular area to a relative oxygen saturation were the same as for the visible spectrum oxygen-sensitive triangles.

RESULTS

Visualization

Comparing figures 17 and 18 shows that the choroid is much less visible in the visible spectrum images of a healthy control (Figure 17) than images of a different healthy control taken with NIR wavelengths (Figure 18). The same difference can be seen when comparing the visible spectrum images of a 79 year old white, non-Hispanic female wet AMD patient with the images of this same patient taken with NIR wavelengths (Figures 19 and 20).

Oxygen saturation

All results are summarized in Table 3. The results from the visible spectrum images are as follows. The average oxygen saturation for the ONH cup was 65 ± 6 percent for healthy controls and 61 ± 10 percent for glaucoma patients. The difference between the groups as a percentage of the healthy oxygen saturation was 7 percent. The average oxygen saturation for the ONH rim was 67 ± 3 percent for healthy controls and 64 ± 17 percent for glaucoma patients. The difference between the groups as a percentage of the healthy oxygen saturation was 4 percent. The average oxygen saturation for the vein overlying the optic disc was 67 ± 15 percent for healthy controls and 56 ± 22 percent for glaucoma patients. The difference between the groups as a percentage of the healthy oxygen saturation was 16 percent. The average oxygen saturation for the macula was $87 \pm$

10 percent for healthy controls and 93 ± 1 percent for glaucoma patients. The difference between the groups as a percentage of the healthy oxygen saturation was 7 percent in the positive direction. This was the only area analyzed that exhibits higher average oxygen saturation in the glaucoma group than in the healthy control group.

The results from the NIR images are as follows. The average oxygen saturation from the vein was 66 ± 20 percent for healthy controls, 58 ± 0.4 percent for glaucoma suspects and 54 ± 17 percent for glaucoma patients. The difference between the healthy control and glaucoma suspect groups as a percentage of the healthy oxygen saturation was 12 percent. The difference between the glaucoma suspect and the glaucoma groups as a percentage of the glaucoma suspect group oxygen saturation was also 12 percent. The total difference between the healthy control and glaucoma groups as a percentage of the healthy oxygen saturation was 19 percent.

The NIR images analyzed to probe the choroidal tissue below the macula yielded 99 ± 5 percent in healthy controls and 81 ± 8 percent in glaucoma patients. The difference between the groups as a percentage of the healthy oxygen saturation was 18 percent.

The difference between 96 percent saturation of an ideal artery and the individual oxygen saturation averages for the areas analyzed are listed in Table 4. The visible spectrum vein oxygen saturation average was 29 percent lower than 96 percent saturation of an artery for healthy controls and 40 percent lower for glaucoma patients. The NIR region vein oxygen saturation average was 30 percent lower than 96 percent saturation of an artery for healthy controls, 32 percent lower for glaucoma suspects and 38 percent lower for glaucoma patients. The visible spectrum ONH cup oxygen saturation average

was 31 percent lower than 96 percent saturation of an artery for healthy controls and 35 percent lower for glaucoma patients. The visible spectrum ONH rim oxygen saturation average was 29 percent lower than 96 percent saturation of an artery for healthy controls and 32 percent lower for glaucoma patients. The visible spectrum macula oxygen saturation average was 9 percent lower than 96 percent saturation of an artery for healthy controls and 3 percent lower for glaucoma patients. The NIR region choroid oxygen saturation average was 3 percent higher than 96 percent saturation of an artery for healthy controls and 15 percent lower for glaucoma patients. The difference was consistently more pronounced in the glaucoma groups with the exception of the difference in the macula. The NIR vein oxygen saturation average differences from 96 percent saturation of an artery were gradually more pronounced from healthy controls to glaucoma suspects to glaucoma patients. All oxygen saturation values were less than 96 percent saturation of an artery except for that of the choroid in healthy controls, which looks equivalent.

DISCUSSION

There was no obvious qualitative effect of age, race, gender or pathology on the optimal wavelength region for choroidal visualization. The NIR images exhibited enhanced choroidal visibility as assessed qualitatively. The two healthy control images from the different wavelengths are unfortunately from different patients. The two images shown from the AMD patient are matched to the same patient, but are unfortunately taken from different angles. Regardless, it is clear that the NIR wavelengths augment choroidal visibility. This was predicted based on the ability of NIR wavelengths to escape absorption by the RPE.

Khoobehi et al.³⁶ have shown oxygen saturation to decrease in the optic nerve head rim before the optic nerve head cup in healthy monkey retinas sustaining increasing IOP levels. In the case of acute IOP in healthy tissue, autoregulation causes an increase in blood flow and a resistance to changes in oxygen levels. In the case of glaucoma, there is tissue death and autoregulation is impaired.³⁷ This study therefore sought to find evidence of the differential effect on the ONH rim and cup in glaucomatous eyes. The results suggest that the ONH cup is more profoundly affected than the ONH rim in this case, as determined by a larger difference in oxygen saturation between glaucoma patients and healthy controls for the cup than the rim. This also may be due to harsher effects of pressure on the ONH cup, causing it to visibly bulge as shown in Figure 21. Typically, the ONH cup is observed to cup inwards in the posterior direction, so images

detecting an outward, anterior bulge may suggest different underlying physiological causes of the ONH cup pathology. Regardless, the cup seems more susceptible to physical deformation caused by increasing IOP. The difference in effects seen between the healthy monkey retinal tissue and glaucomatous human tissue is likely due to decreased metabolic activity in glaucomatous tissue and impaired autoregulation.

The oxygen saturation in the ONH cup, ONH rim, and vein within the optic disc all were lower in glaucoma patients. These results are consistent with increased IOP leading to decreased ability of the tissue to extract oxygen delivered by the arteries. The increased pressure in the eye may also physically force oxygen out of these structures and into the fluid portion of the eye.

The macula results from the visible spectrum images did not show lower oxygen saturation in the case of glaucoma, and actually showed higher values. This system relies on information from hemoglobin and there is no hemoglobin spectral signature from the avascular macula in the retina. The visible spectrum images may detect the oxygen levels at the very top of the choroid, explaining the increase in the case of glaucoma. When increased IOP causes retinal tissue damage, the tissue is deficient in extracting oxygen from the retinal vasculature. The choroid tries to compensate by delivering oxygen to the suffering retinal tissue. The most superficial layer of the choroid nearest the RPE may therefore exhibit higher oxygen saturation due to a gradient increasing towards the retinal tissue. The most scleral choroidal layer would therefore show lower oxygen saturation. The oxygen saturation calculations from the same area underlying the macula in the monochromatic images from the NIR region did reveal lower oxygen

saturation in glaucoma patients. These findings are thought to reflect the hemoglobin status at the level of the deep choroid.

The difference in oxygen saturation between 96 percent saturation of an artery and the ONH cup, ONH rim, superficial vein, deep vein, and choroid were all more pronounced for the glaucoma patient group than for the healthy control group. The tissue differences may suggest that there is more oxygen left in the arteries due to less extraction by the glaucomatous tissue than by healthy tissue. This suggests a lowered metabolism of retinal tissue in the case of glaucoma, which causes retinal cell death. The vein differences may suggest oxygen diffusion out of the veins into the vitreous humor. In the case of increased IOP, the blood velocity is slowed, which increases the probability of oxygen diffusion away from the vessels (ocular blood flow in glaucoma, Lambrou & Greve). Oxygen in arteries may diffuse into veins due to proximity. This oxygen will not diffuse back into the arteries or into the tissue because the oxygen concentration gradients of both of these structures are unfavorable to diffusion from the veins, where there is the lowest concentration of oxygen. Therefore, it may diffuse into the fluid in the anterior portion of the eye.

Some images were overexposed due to flash settings that are too high or blurry due to imperfect sizing and setting of the filters. If these issues are overcome, the other monochromatic images may be of better quality. Images were not separated based on quality, so the data may reflect this. Engineering of the system should be made more precise for future studies.

Though the sample sizes are small and there is much variability in results, the findings consistently show lower oxygen saturation in glaucoma patients. In the future, a

larger sample size would help determine whether or not these preliminary findings of our pilot study are valid. There are outliers in our results that would skew results from a larger sample to a lesser extent. The large variation within groups may be minimized by adding subjects and by separating the glaucoma patients based on severity of pathology, with primary open angle glaucoma being the most severe. This was not achieved by this study because there were too few patients.

Additionally, the healthy controls were different individuals from the glaucoma patients, as opposed to the same individuals before and after glaucoma onset. If oxygen saturation calculation became a routine measure, the saturation index of glaucoma patients may be compared to their pre-glaucoma indices. However, there are many functional and physiological changes of the fundus due to aging that may not be controlled for in these comparisons.

The data from the superficial fundus layers as imaged with visible wavelengths and the deeper layers as imaged with NIR region wavelengths were also from different subjects. Ideally, a system would be engineered with two sets of bandpass filters that may be switched quickly between image acquisitions. In this scenario, a clinician could obtain optical information about and oxygen saturation of the more superficial retina as well as deeper layers of the fundus.

Lastly, as seen in Figure 16, variable blood perfusion affects the penetration depth at a given wavelength. Because autoregulation is impaired in glaucoma patients and there is decreased ocular blood flow, this may lead to different penetration depths at the same wavelength for healthy controls and glaucoma patients. This would confound the

comparison. Future studies should pair oxygen saturation measurements with blood flow measurements, assessed by Laser Doppler Flowmetry.

APPENDICES

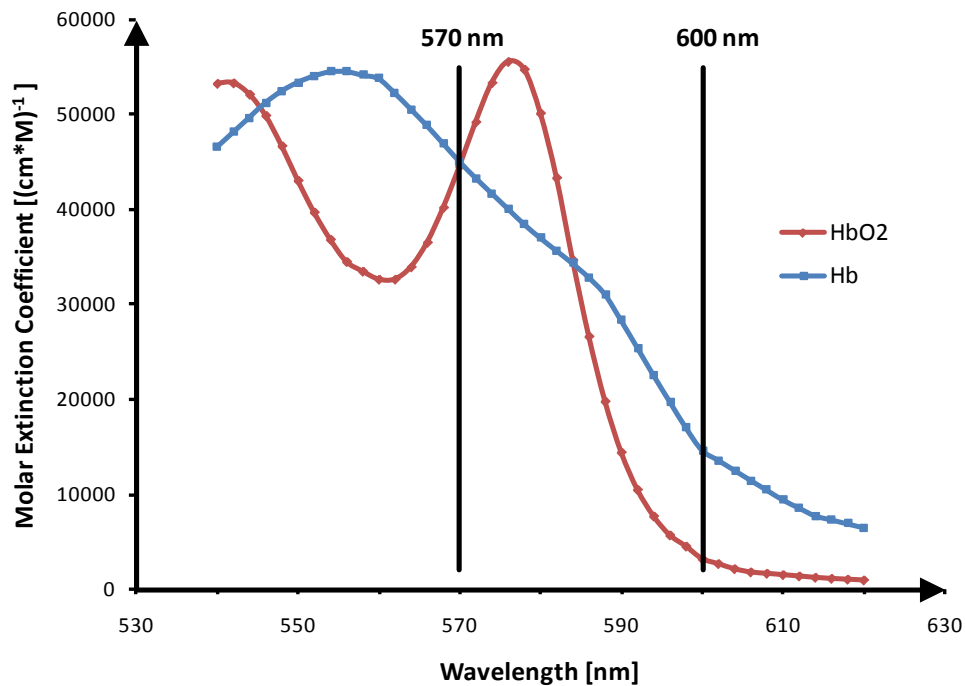


Figure 1: Spectral curves for oxyhemoglobin (HbO₂) and deoxyhemoglobin (Hb). These curves show an isosbestic, or oxygen-insensitive, wavelength at 570 nm and an oxygen-sensitive wavelength at 600 nm. The molar extinction coefficient is directly proportional to absorption. The absorption of 570 nm light is the same for Hb and HbO₂. The absorption difference between Hb and HbO₂ is at a maximum at 600 nm. The ratio between the optical density in the image at 570 nm and the optical density of the image at 600 nm is proportional to hemoglobin oxygen saturation.

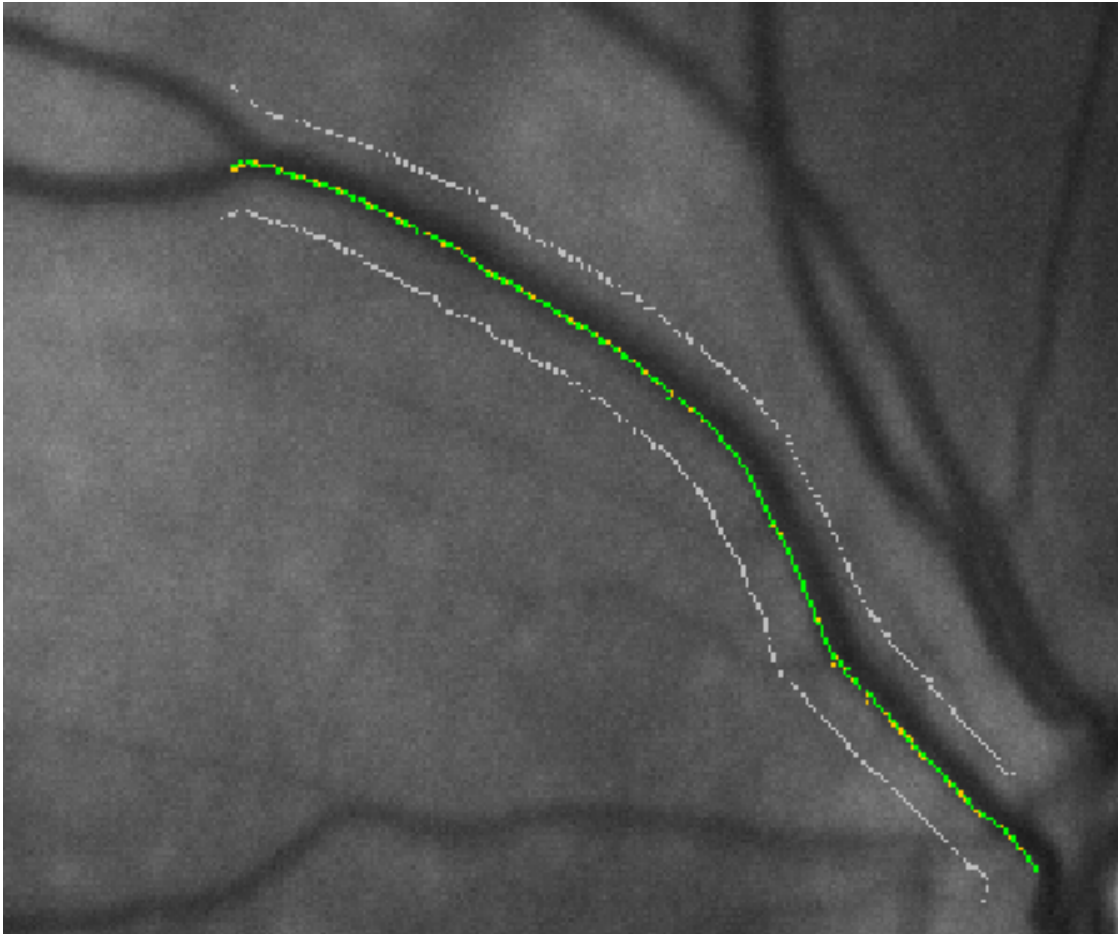


Figure 2: Image depicting intensity point selections from within and outside a vessel. The optical density of a vessel at a specific wavelength is determined by dividing the intensity within the vessel by the intensity of the tissue just outside the vessel, which normalizes the value to local conditions. The original light intensity is approximated by the intensity from the tissue outside the vessel.

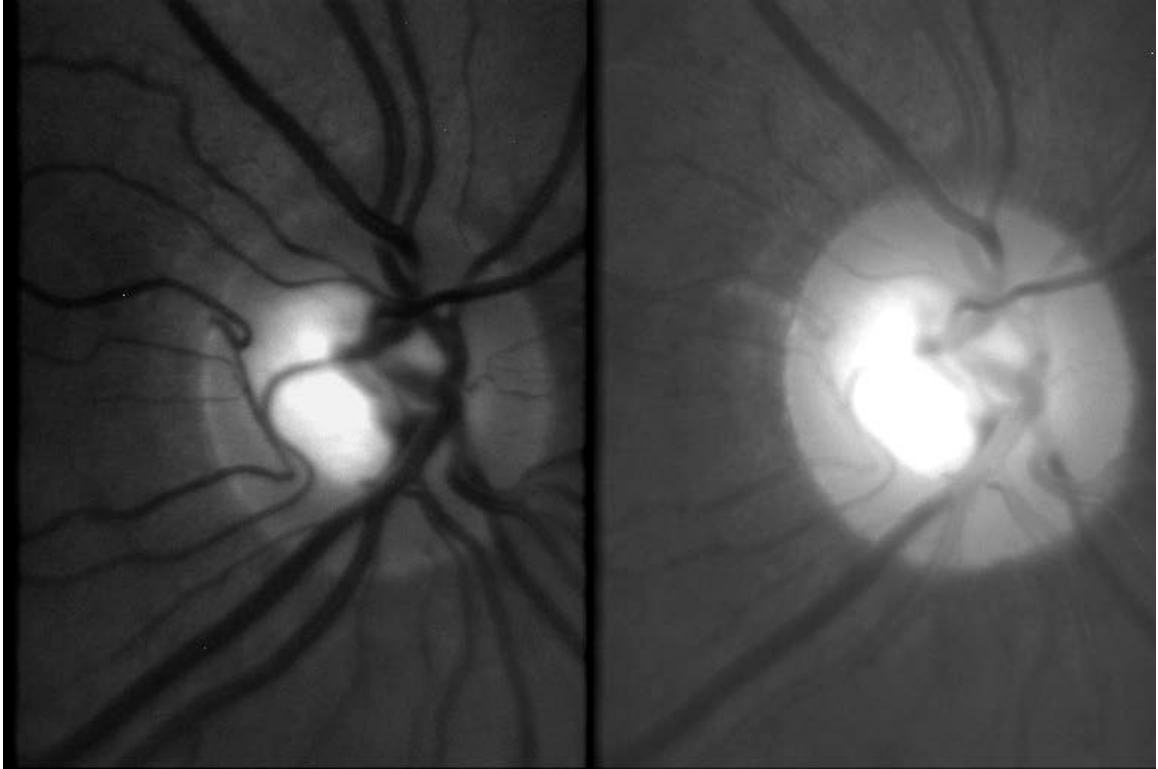


Figure 3: Monochromatic images of the optic nerve head taken at 570 nm and 600 nm.

The monochromatic image at 570 nm, on the left, lacks resolution between arteries and veins because oxyhemoglobin (HbO_2) and deoxyhemoglobin (Hb) absorb the same amount of this wavelength. However, the monochromatic image at 600 nm, on the right, exhibits resolution between arteries and veins because there is a maximum difference between the absorption of this wavelength of light by Hb and by HbO_2 .



Figure 4: Monochromatic images of the retina taken at 570 nm and 600 nm. Comparison of these images also shows that there is resolution of arteries and veins in the monochromatic image at 600 nm, on the right, but not at 570 nm, on the left. The lighter vessel in the right image is an artery. Arterial blood is highly oxygenated and this oxygen causes the blood to turn red. Therefore, arterial blood will reflect wavelengths in the red region of visible light. Veins, on the other hand, will reflect wavelengths corresponding to blue light because deoxygenated blood is blue.

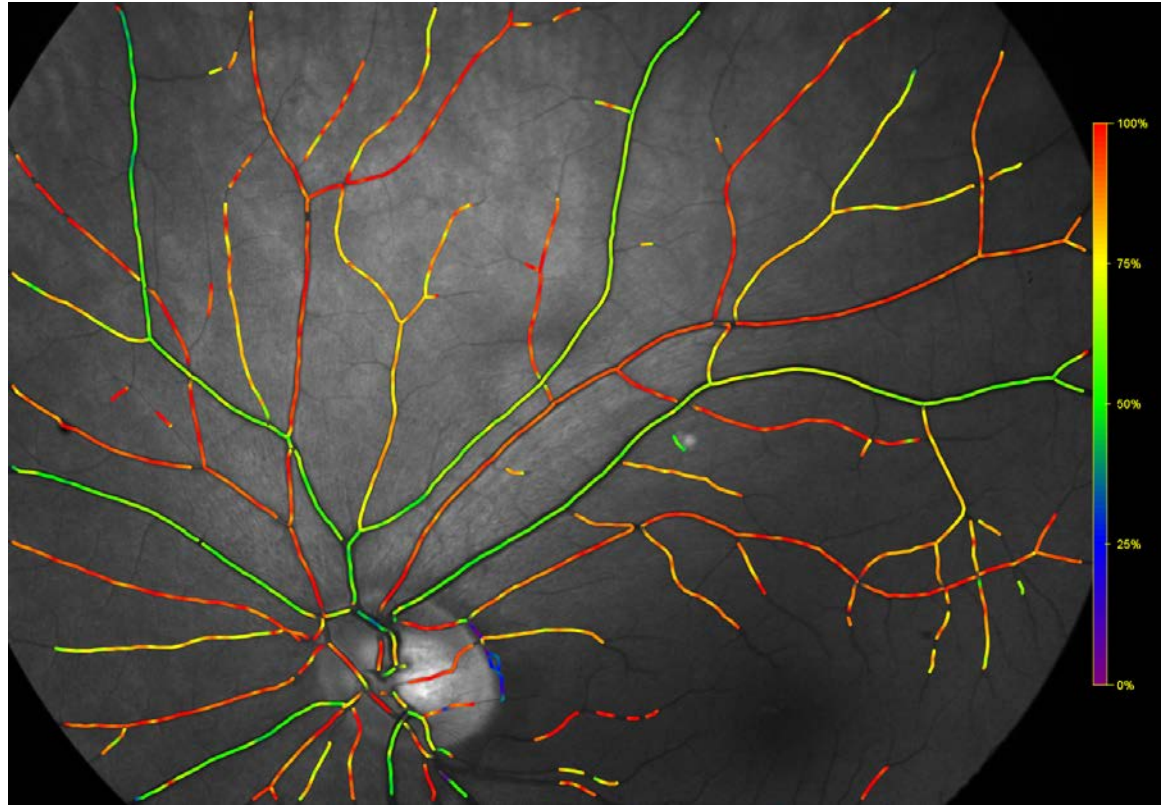


Figure 5: Monochromatic fundus image at 570 nm with an oxygen saturation overlay.

This image was taken from a healthy volunteer. The colors represent the estimate of oxygen saturation based on the optical density ratio between the images at 570 nm and 600 nm. Higher oxygen saturation is indicated by red and lower oxygen saturation is indicated by blue. The color bar on the right shows the percent oxygenation associated with the different colors. A clear difference between arteries and veins is shown. Arteries are more red while veins are more green.

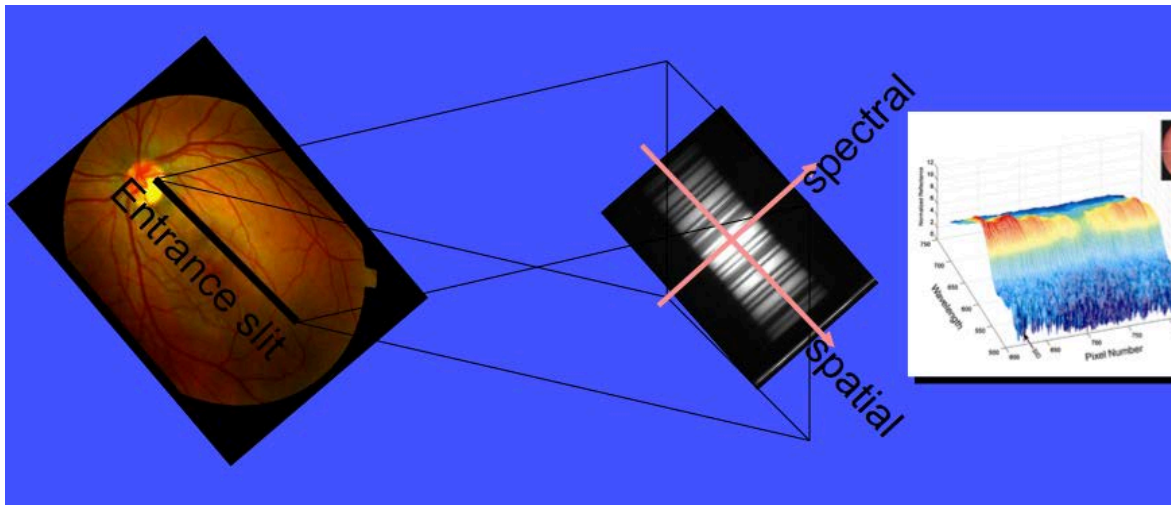


Figure 6: Schematic of hyperspectral imaging acquisition. A single spatial line of the image is acquired by the spectrometer at a time. Complete spectral information is acquired for each point along each individually acquired spatial lines. The system takes approximately 8 seconds to scan the entire fundus. Anesthetized monkeys have been scanned with this system to prevent blurring of the image due to saccadic eye movement.

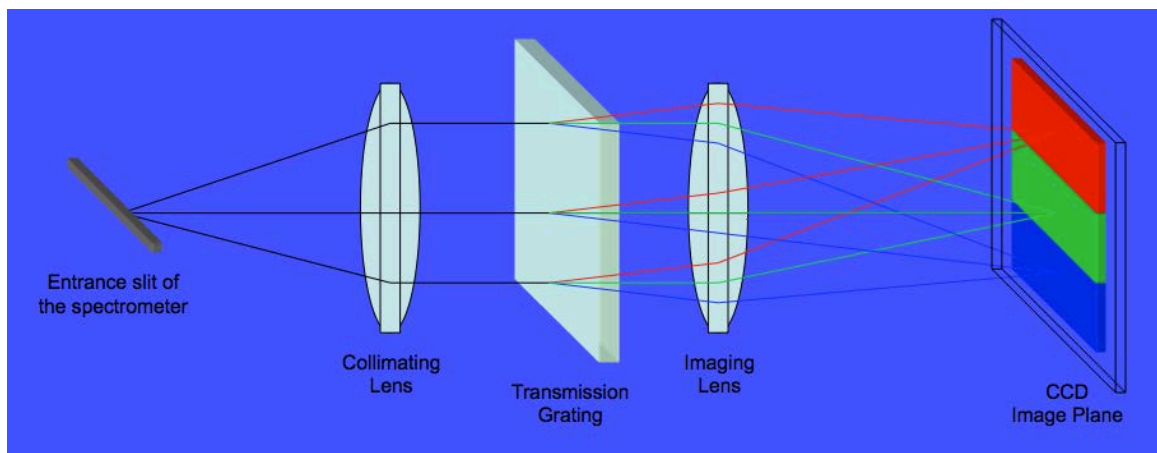


Figure 7: Schematic of the hyperspectral imaging design. The slit of spectral information is collimated by the first before passing through a transmission grating. The imaging lens then focus the image slit onto a charged coupled device image plane and the data is recorded.

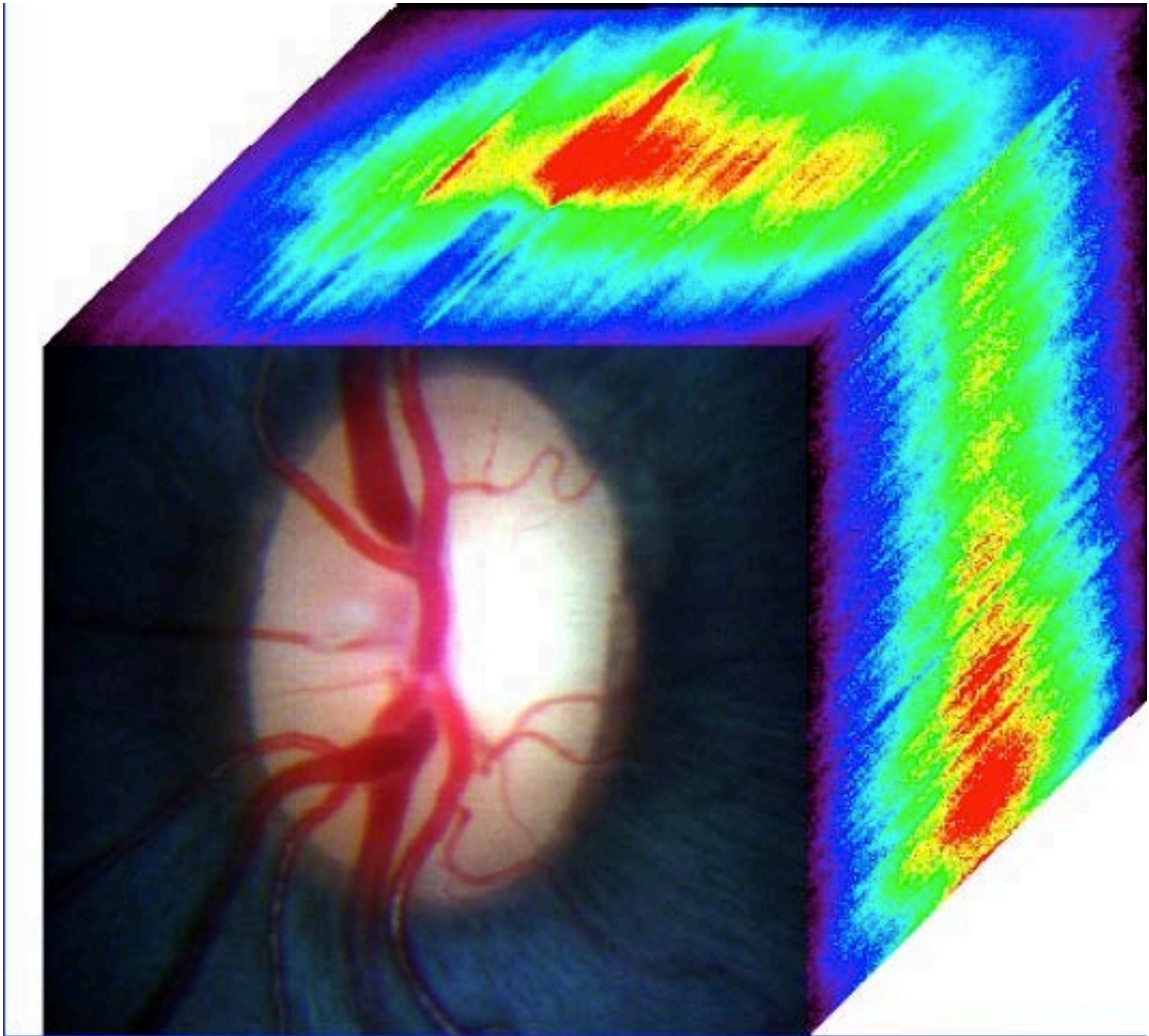


Figure 8: Hyperspectral image cube. This cube was created from the data obtained by the scanning hyperspectral imaging system. This figure appears three dimensional, but it actually encodes four dimensional data. There is relative reflected light intensity data encoded for 2 dimensional spatial coordinates at each individual wavelength of the visible spectrum. Wavelength versus reflected light intensity plots may then be created for each point in an image. Alternatively, the average reflected light intensities from areas of interest may also be plotted against wavelength.

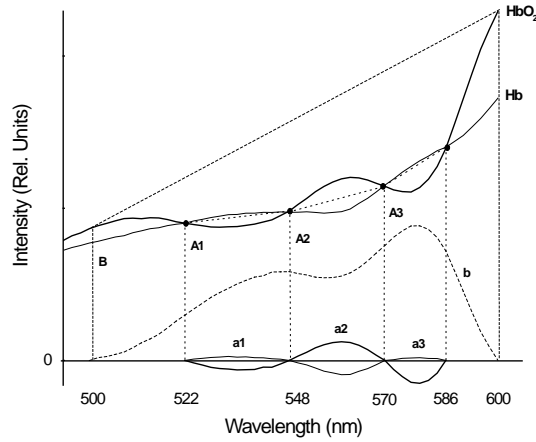


Figure 9: Graphical depiction of Khoobehi et al.'s saturation algorithm. Three regions between the spectral reflectance curves for oxyhemoglobin (HbO_2) and deoxyhemoglobin (Hb) are bound by isosbestic points of equal light absorption. Areas between adjacent isosbestic points and line segments connecting them are proportional to oxygen saturation. Areas below line segments connecting adjacent isosbestic points, labeled A1, A2, and A3, are sensitive to total reflected light intensity of each area. The curves after subtracting the light sensitive areas are re-plotted on the x-axis and labeled a1, a2, and a3. The oxygen sensitive component (OSC) is a combination of saturation-dependent terms after compensating for total light intensity:

$$\text{OSC} = a2 / A2 - a1 / A1 - a3 / A3.$$

The area between the hemoglobin spectral curve and the long line segment connecting isosbestic points at 522 and 586 nm, labeled b in the figure, varies directly with blood volume. The area under the long segment, labeled B in the figure, is proportional to total light intensity within this spectral segment. The blood volume component (BVC) normalized to total light intensity is defined as b / B . The volume-corrected relative saturation index is: $\text{RSI} = \text{OSC} / \text{BVC}$.

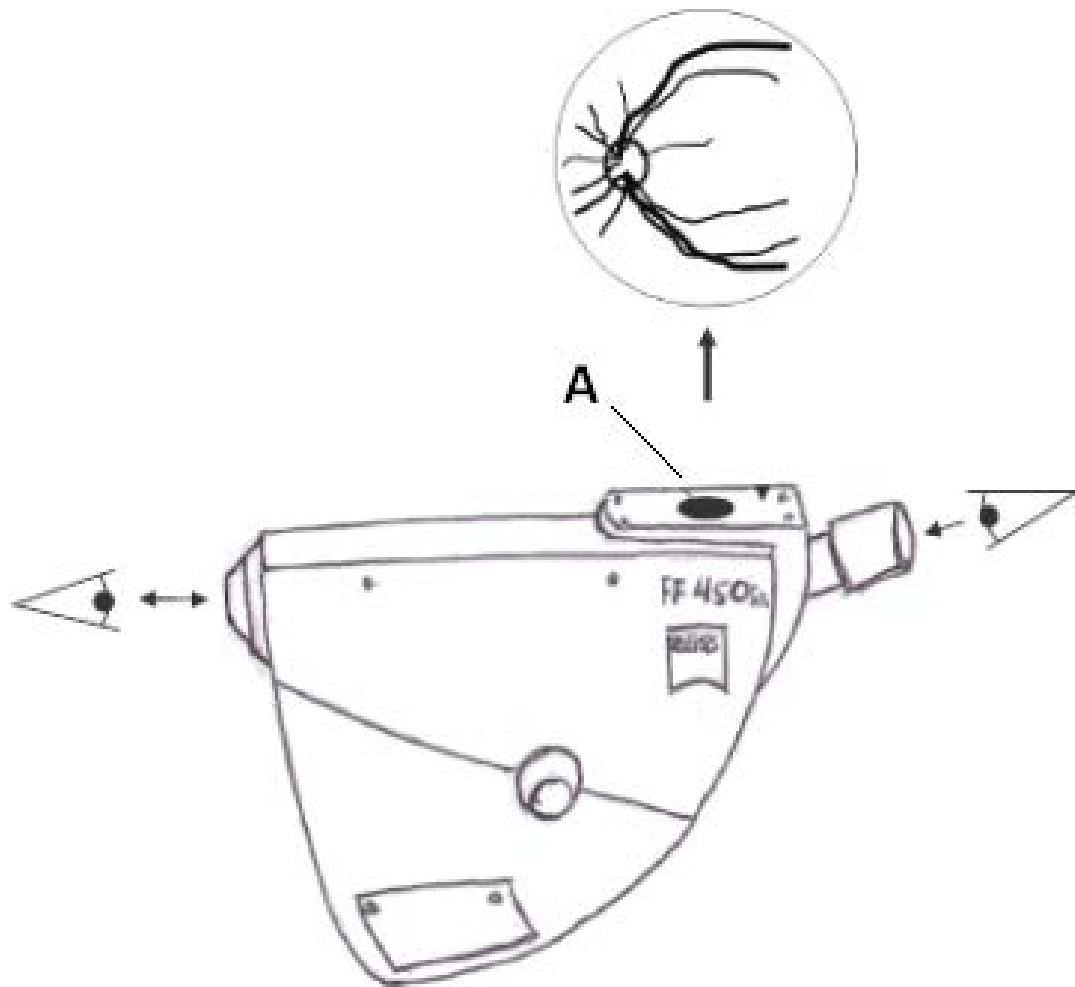


Figure 10: Schematic of the fundus camera Zeiss FF450 IR. A traditional fundus camera flash is utilized. The reflectance data acquired leaves the exit pupil, labeled A in the figure, and is subsequently separated to produce seven monochromatic images as illustrated in Figure 11.

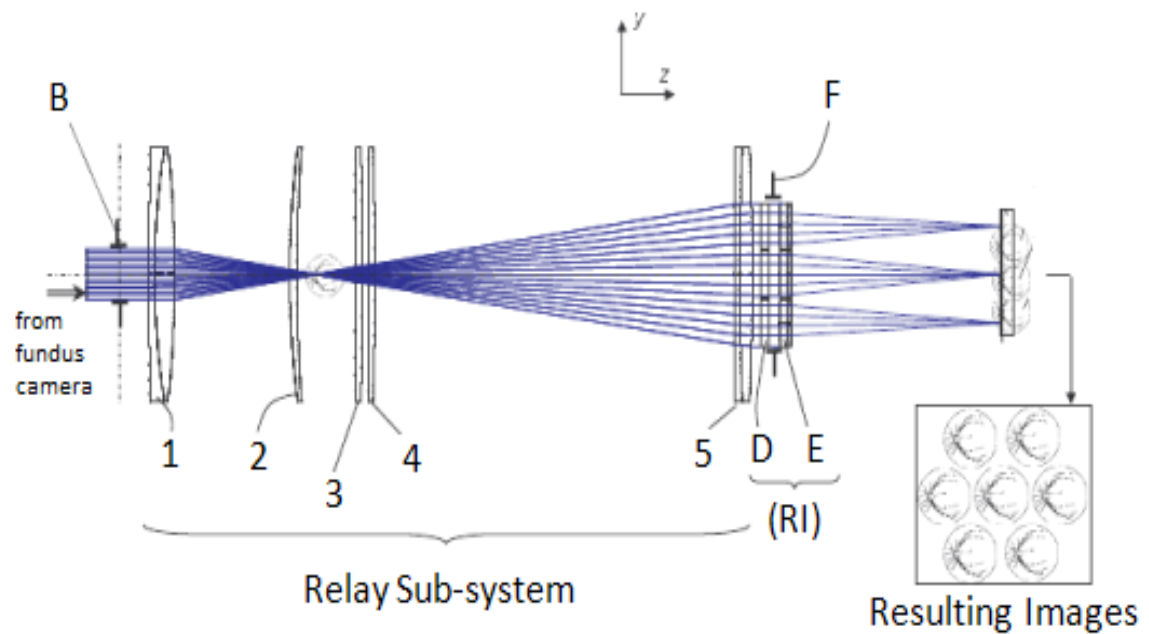


Figure 11: Schematic of the relay sub-system and reimaging lenses. The reflected light passes through these lenses after leaving the exit pupil of the fundus camera. Lenses 1 and 2 in the figure focus the light. Lenses 3 and 4 enlarge the image before the light is collimated by lens 5. D and E reimage the light to produce seven monochromatic images.

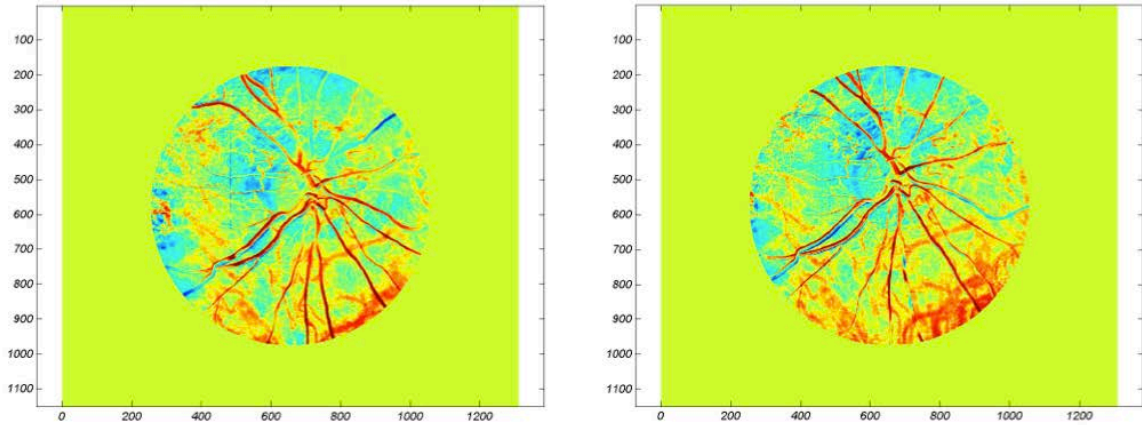


Figure 12: Evidence of reproducibility. Two oxygen saturation maps from the same healthy control on two separate days show roughly the same oxygenation patterns. The relative oxygen saturation is color-coded from blue (low) to red (high).

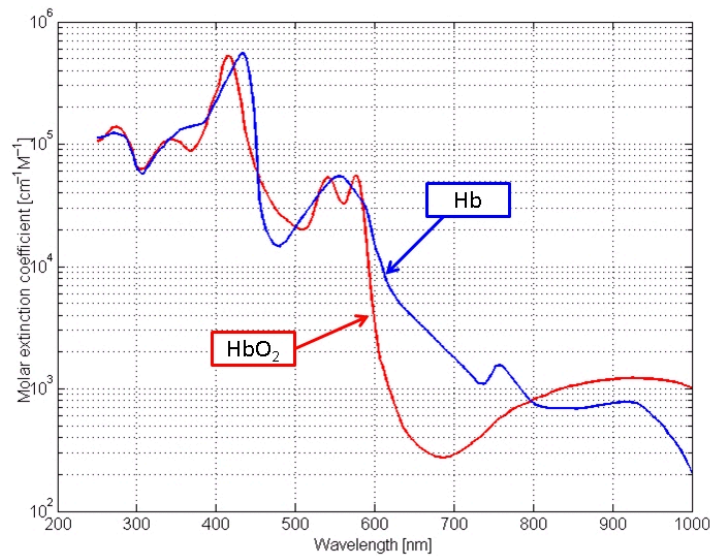


Figure 13: Expanded view of the oxyhemoglobin (HbO_2) and deoxyhemoglobin (Hb) curves. The area of interest in the visible spectrum from 522 nm to 586 nm encompasses three oxygen saturation-sensitive areas between the HbO_2 and Hb curves. There is only one area between the curves to approximate in the longer wavelength, near infrared region.

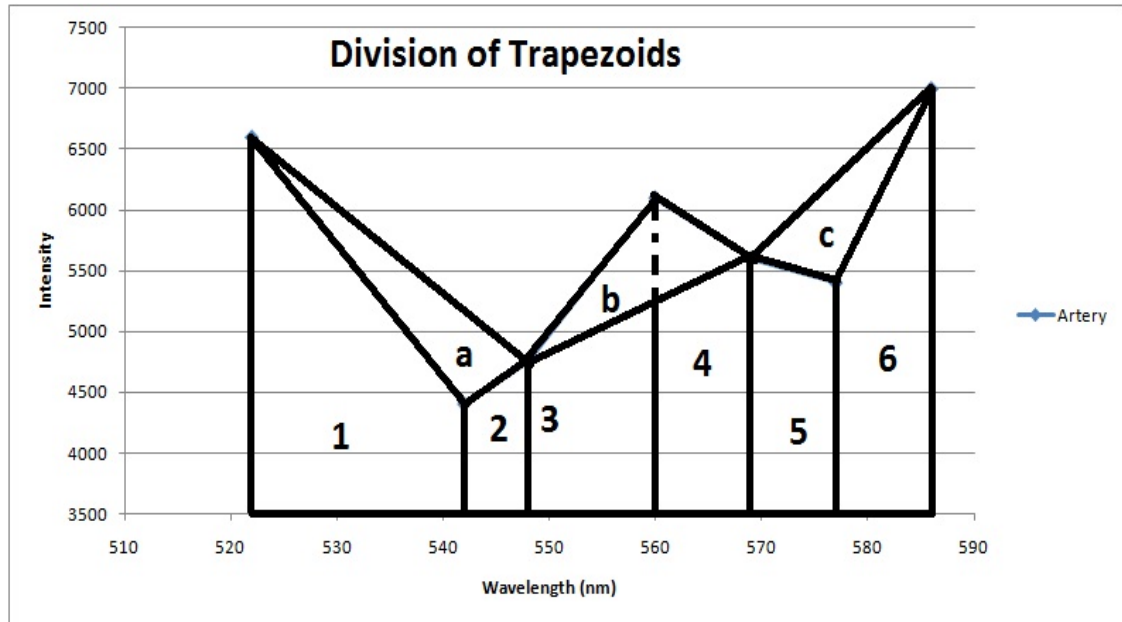


Figure 14: Division of trapezoids in the oxygen saturation index algorithm. The same calculations made from the hyperspectral imaging data can be made from data at seven discrete wavelengths from the multispectral imaging system. Areas a, b, and c are proportional to oxygen saturation and areas 1, 2, 3, 4, 5, and 6 are sensitive to total reflected light intensity.

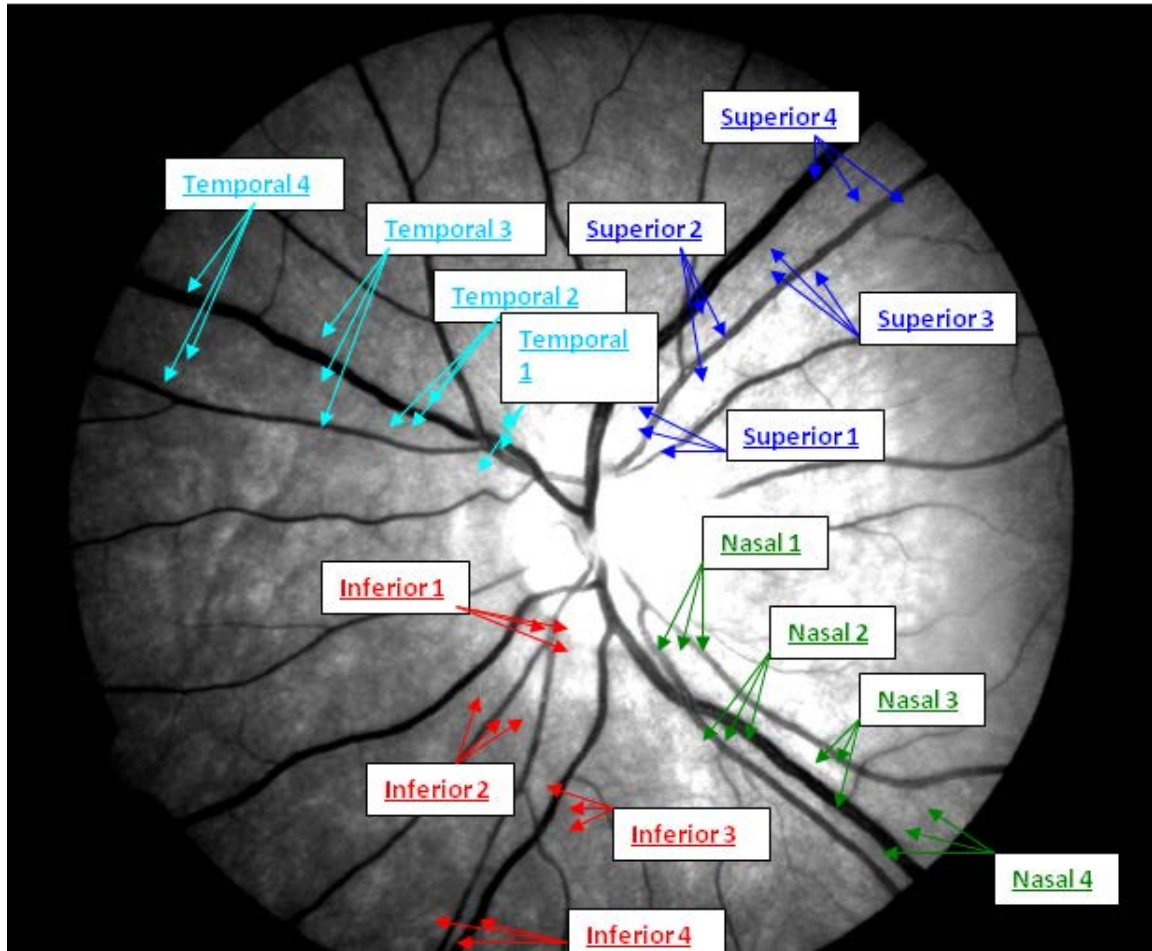


Figure 15: Image key identifying analyzed areas around the optic nerve head. These areas were analyzed for oxygen saturation. An area from within a vein and an area of adjacent tissue were analyzed in the area just outside the optic nerve head (ONH), an area 1.5 ONH radii away, an area 2.5 ONH radii away, and an area 3.5 ONH radii away.

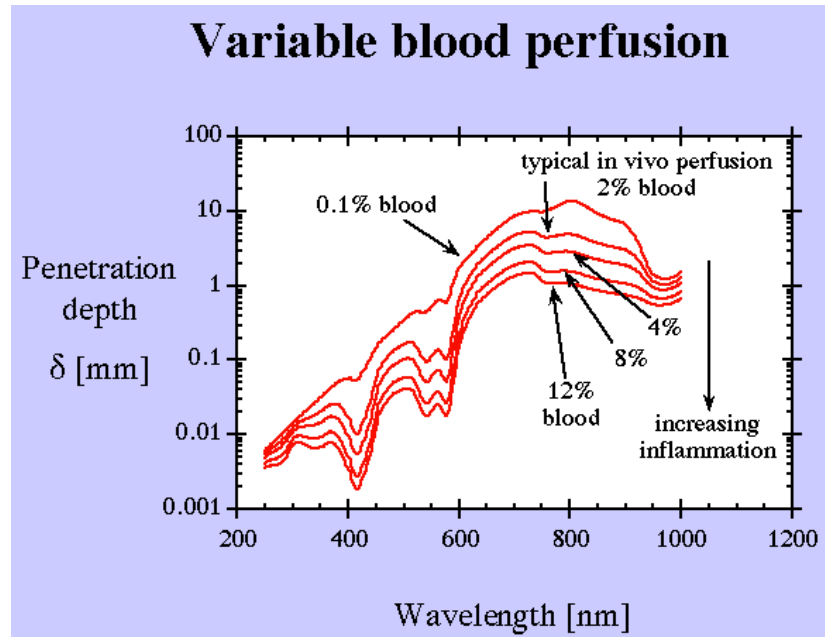


Figure 16: Penetration depth in millimeters as a function of both variable blood perfusion and wavelength in nanometers. Longer wavelengths tend to exhibit higher penetration depths and higher blood perfusion tends to decrease the penetration depth.

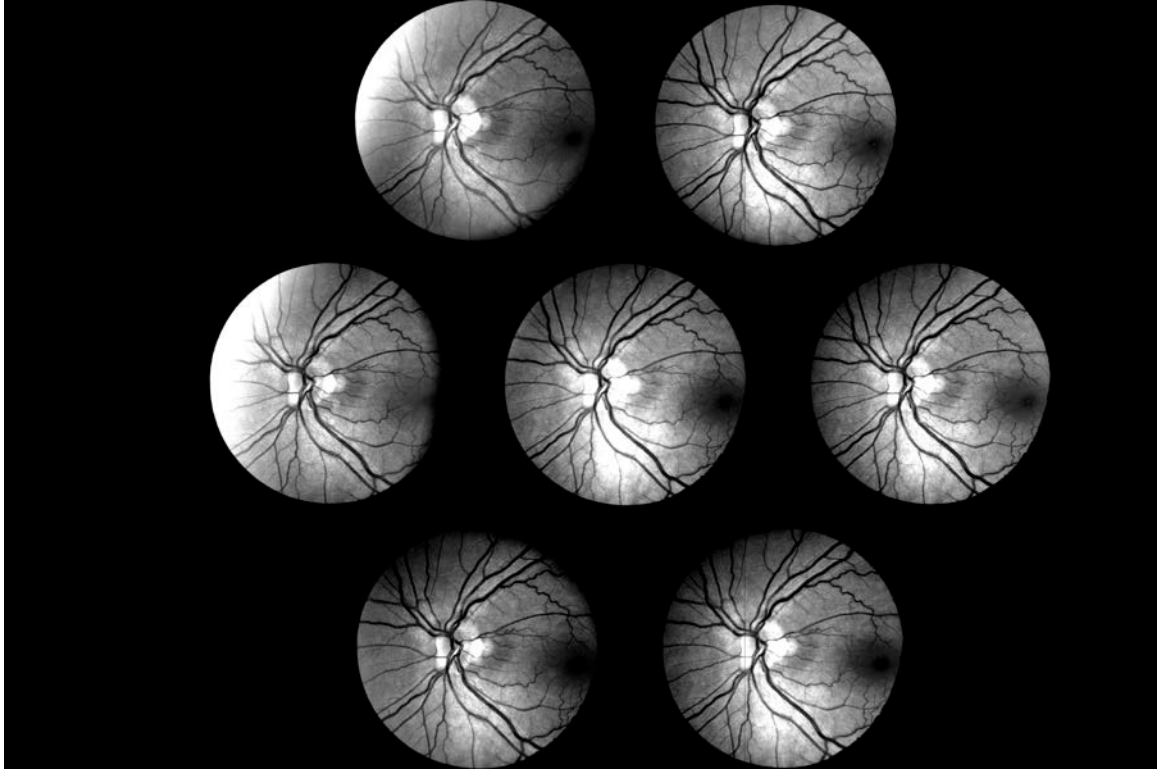


Figure 17: Images from a healthy control using visible wavelengths. These images were captured using the multispectral imaging system. The optic nerve head is visible near the center of each image. The macula is visible on the right side of each image. The 16-bit charged coupled device digital camera is sensitive enough to detect the spectral intensity differences between each monochromatic image. The penetration depth in the visible spectrum is at the level of the retinal vessels and tissue and the superficial optic nerve.

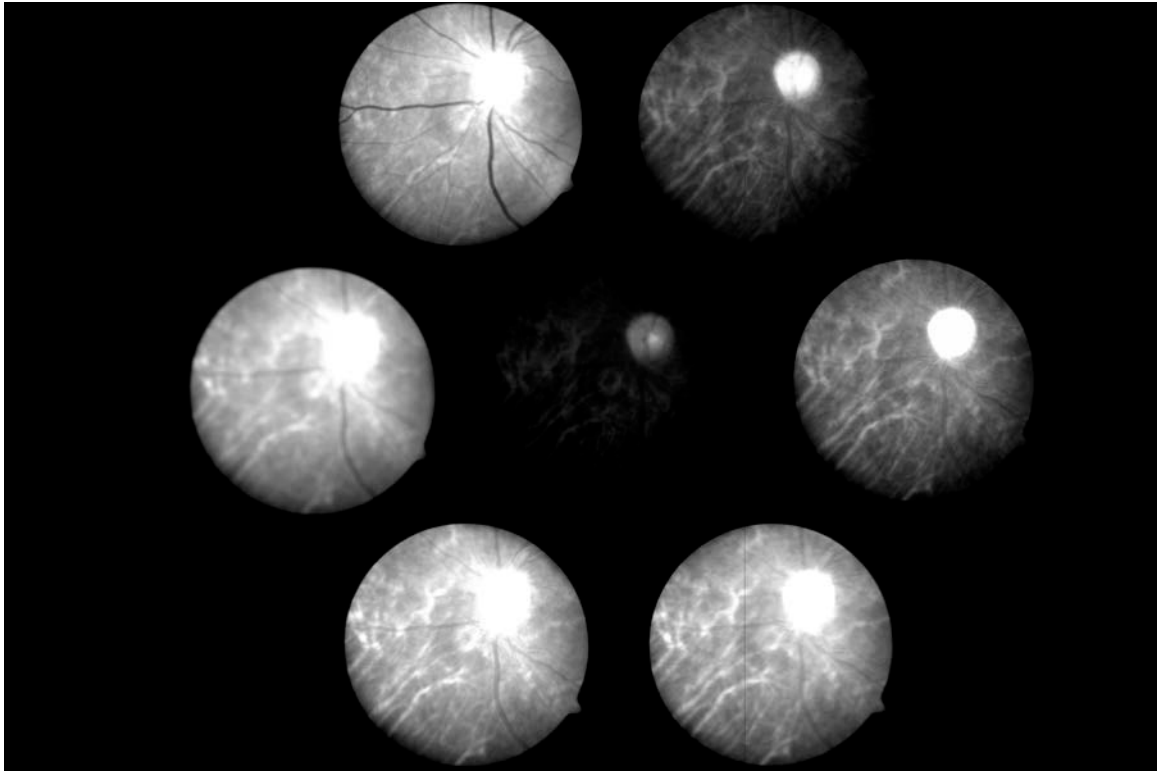


Figure 18: Images from a healthy control using near infrared (NIR) wavelengths. These images were captured using the multispectral imaging system. The optic nerve head can be seen in the top right quadrant of each image. The 16-bit charged coupled device digital camera is sensitive enough to detect the spectral intensity differences between each monochromatic image. The penetration depth in the NIR region is at the level of the choroid and the level of the optic nerve at the same depth.

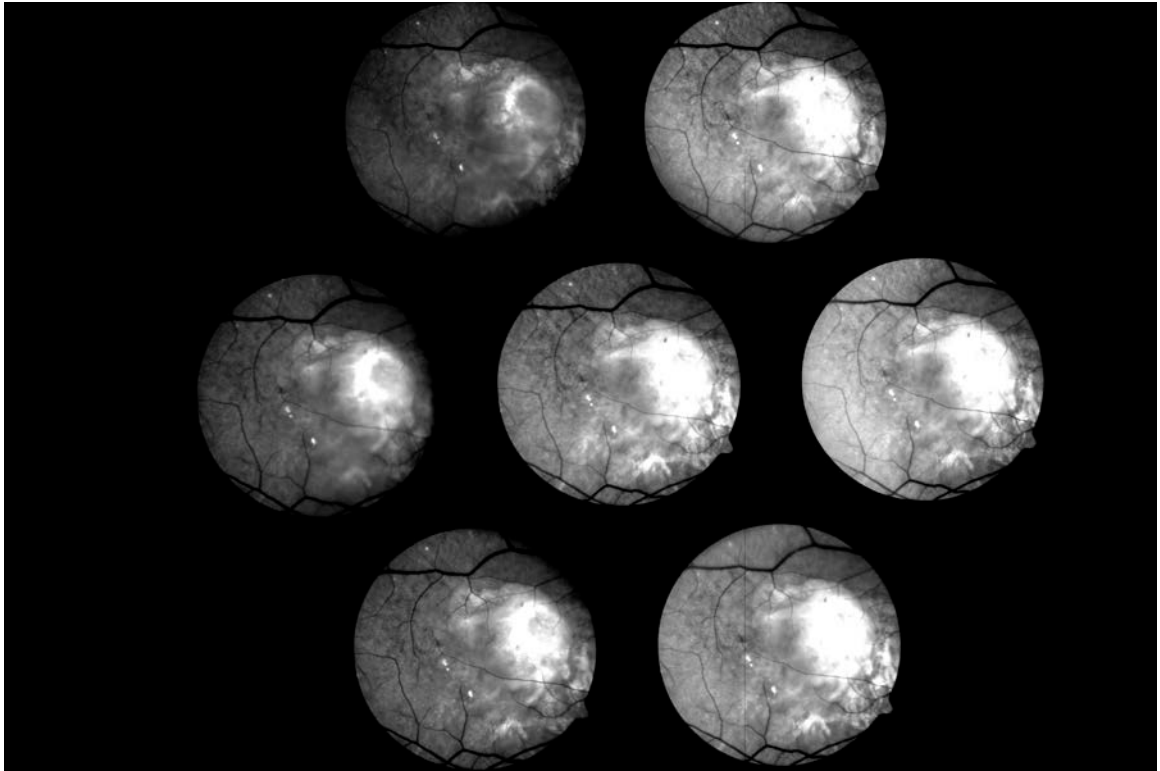


Figure 19: Images from a wet age-related macular degeneration patient using the multispectral imaging system with visible wavelengths. The macula is visible on the right side of the image. Increased intensity is seen due to degeneration of macular tissue and neovascularization below this area. There is a limited amount of choroidal visibility apparent because this patient is light-skinned and thus has a light retinal pigment epithelium that lets some visible light pass.

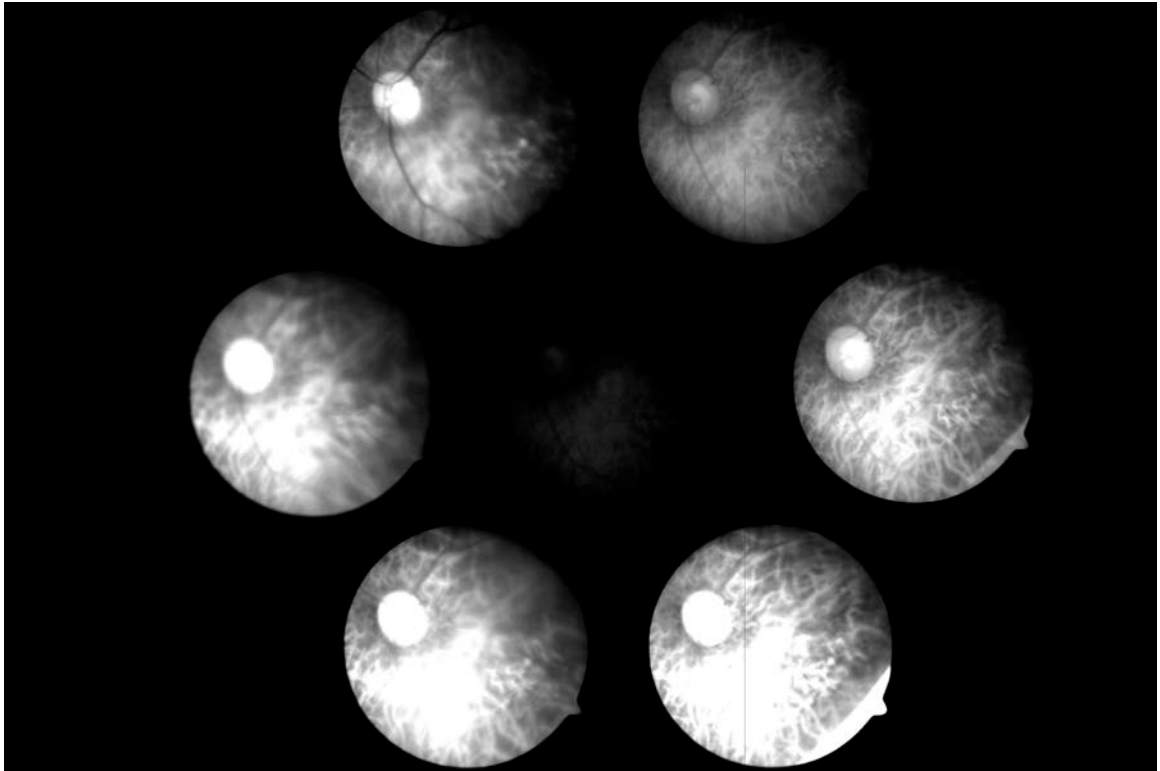


Figure 20: Images from the wet age-related macular degeneration patient from Figure 19 using the multispectral imaging system with near infrared (NIR) wavelengths. This image is from a different angle than the image in Figure 19, so the optic nerve head is visible here but not the macula. Enhanced choroidal visibility above that of the images in Figure 19 are seen due to enhanced penetration depth of the NIR wavelengths.

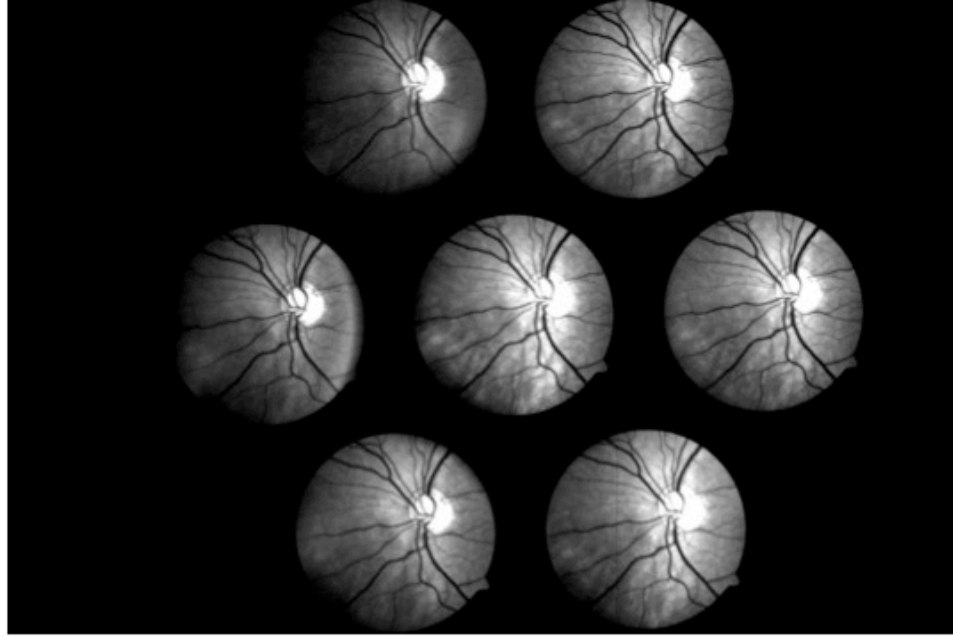


Figure 21: An image of a glaucoma patient exhibiting bulging of the optic nerve head (ONH) cup. Typically glaucoma patients exhibit an inwards cupping of the ONH cup in the posterior direction. A few images in this study showed bulging outwards of the ONH cup in the anterior direction. This may be indicative of a different physical and physiological course of the disease in a subset of patients.

Temporal Vein		Inferior Vein		Nasal Vein		Superior Vein	
Average	SD	Average	SD	Average	SD	Average	SD
62%	7%	63%	4%	63%	4%	54%	3%
Temporal Tissue		Inferior Tissue		Nasal Tissue		Superior Tissue	
Average	SD	Average	SD	Average	SD	Average	SD
77%	4%	76%	3%	74%	2%	77%	4%

Table 1: Oxygen saturation results from the retinal areas shown in Figure 15. The percent oxygen saturation was calculated by comparing the intensities to that of an arterial area, which was set to correspond to 96 percent saturation. The vein oxygen saturation values are much lower and the tissue oxygen saturation values are intermediate between the vessels.

Glaucoma patients: Visible vein, ONH cup, ONH rim		Healthy controls: Visible vein, ONH cup, ONH rim	Glaucoma patients: Visible macula
Age range	53-87 years	29-50 years	64-87 years
Average age	67 years	40 years	72 years
White, non-Hispanic	3	9	1
African American	3	1	3
Female	4	10	3
Male	2	0	1
Healthy controls: Visible macula		Glaucoma patients: NIR vein	Glaucoma suspects: NIR vein
Age range	29-48 years	63-81 years	65-68 years
Average age	39 years	71 years	67 years
White, non-Hispanic	9	2	1
African American	0	8	1
Female	9	6	1
Male	0	4	1
Healthy controls: NIR vein		Glaucoma patients: NIR choroid	Healthy controls: NIR choroid
Age range	41-70 years	59-79 years	41-76 years
Average age	58 years	70 years	60 years
White, non-Hispanic	1	1	2
African American	2	5	3
Asian (dark Filipino)	1	0	1
Female	3	4	4
Male	1	3	2

Table 2: Demographic data. Age range, average age, race, and gender were recorded for all subjects in the following groups analyzed for oxygen saturation. No qualitative effect of any of these variables was observed. The only variable consistently lowering oxygen saturation was glaucoma status.

	Healthy controls		Glaucoma suspects		Glaucoma patients		Difference as a percent of healthy controls
	Average	SD	Average	SD	Average	SD	
Visible cup	65	6			61	10	7% lower
Visible rim	67	3			64	17	4% lower
Visible vein	67	15			56	22	16% lower
Visible macula	87	10			93	1	7% higher
NIR vein	66	20	58	0.4	54	17	19% lower
NIR choroid	99	5			81	8	18% lower

Table 3: Oxygen saturation results for areas of interest in monochromatic images from the visible spectrum and from the NIR region. The percent difference between healthy controls and glaucoma patients is listed in the last column. In every area analyzed except the macula, glaucoma patients had lower oxygen saturation than healthy controls. The calculation is based on the oxyhemoglobin spectral curve, but the avascular macula lacks hemoglobin. The higher oxygen saturation seen in glaucoma patients may be due to oxygen saturation difference at the most anterior portion of the choroid. The vein oxygen saturation at the penetration depth imaged by the NIR region wavelengths employed were 12 percent lower for glaucoma suspects than for healthy controls and another 12 percent lower for glaucoma patients than for glaucoma suspects. This shows a progressive difference between groups, possibly supporting the idea of a progressive oxygen saturation decrease in patients with worsening pathology.

	Healthy controls	Glaucoma suspects	Glaucoma patients
Visible cup	-31		-35
Visible rim	-29		-32
Visible vein	-29		-40
Visible macula	-9		-3
NIR vein	-30	-32	-38
NIR choroid	+3		-15

Table 4: Differences between oxygen saturation results for the areas of interest and 96 percent saturation of the ideal artery. The oxygen saturation differences from arterial saturation were more pronounced in glaucoma patients than in healthy controls for all areas analyzed except the avascular macula.

LIST OF REFERENCES

1. Rodieck RW. The vertebrate retina: Principles of structure and function. Freeman & Company, W.H (1973). ISBN-10: 0716706962.
2. Polyak SL. The retina. The University of Chicago Press, Illinois; First Edition, Fiftieth Anniversary Publication of Chicago University Press edition (1948). ASIN: B006T5DN8G.
3. Hayreh SS. Anterior ischemic optic neuropathy. Springer-Verlag (1975). ISBN-10: 038706916X.
4. Zhang HR, Gao J, Tian L. The segmental characteristic of the human choroid vessels and its clinical significance. Chin. J. Ophthal. 26: 32-35.
5. Fluorescein Angiography at the US National Library of Medicine Medical Subject Headings (MeSH)
6. Kunitomo, Derek; Kunal Kanitkar, and Mary Makar (2004). The Wills eye manual: office and emergency room diagnosis and treatment of eye disease. (4th ed.). Philadelphia, PA: Lippincott Williams & Wilkins. p. 365. ISBN 978-0781742078.
7. Yannuzzi LA, Slakter JS, Sorenson JA, et al. Digital indocyanine green videoangiography and choroidal neovascularization. Retina. 1992;12(3):191-223. Hua R, Liu L, Wang X, Chen L. Imaging evidence of diabetic choroidopathy in vivo: angiographic pathoanatomy and choroidal-enhanced depth imaging. PLoS One. 2013 Dec 13;8(12):e83494. doi: 10.1371/journal.pone.0083494. eCollection 2013. PubMed PMID: 24349522; PubMed Central PMCID: PMC3862692.
9. Luty GA. Effects of diabetes on the eye. Invest Ophthalmol Vis Sci. 2013 Dec 13;54(14):ORSF81-7. doi: 10.1167/iovs.13-12979. Review. PubMed PMID: 24335073; PubMed Central PMCID: PMC3864380.
10. Saker S, Stewart EA, Browning AC, Allen CL, Amoaku WM. The effect of hyperglycaemia on permeability and the expression of junctional complex molecules in human retinal and choroidal endothelial cells. Exp Eye Res. 2014 Apr;121:161-7. doi: 10.1016/j.exer.2014.02.016. Epub 2014 Mar 2. PubMed PMID: 24594192.
11. Healio Ophthalmology. ICG angiography with PDT useful for serous pigment epithelial detachments. OSN Retina. 2013 Feb.

12. Dhoot DS, Huo S, Yuan A, Xu D, Srivistava S, Ehlers JP, Traboulsi E, Kaiser PK. Evaluation of choroidal thickness in retinitis pigmentosa using enhanced depth imaging optical coherence tomography. *Br J Ophthalmol*. 2013 Jan;97(1):66-9. doi: 10.1136/bjophthalmol-2012-301917. Epub 2012 Oct 23. PubMed PMID: 23093617.
13. Langham ME, Kramer T. Decreased choroidal blood flow associated with retinitis pigmentosa. *Eye (Lond)*. 1990;4 (Pt 2):374-81. PubMed PMID: 2379647.
14. Fromberg I, Krause M, Brückner K, Lang M, Seitz B. [Choroidal effusion after uncomplicated cataract surgery]. *Klin Monbl Augenheilkd*. 2008 Jun;225(6):591-3. doi: 10.1055/s-2008-1027431. German. PubMed PMID: 18516782.
15. Dadaci Z, Doganay F, Oncel Acir N, Aydin HD, Borazan M. Enhanced depth imaging optical coherence tomography of the choroid in migraine patients: Implications for the association of migraine and glaucoma. *Br J Ophthalmol*. 2014 Feb 26. doi:10.1136/bjophthalmol-2013-304711. [Epub ahead of print] PubMed PMID: 24574436.
16. Krantic S, Torriglia A. Retina: source of the earliest biomarkers for Alzheimer's disease? *J Alzheimers Dis*. 2014 Jan 1;40(2):237-43. doi:10.3233/JAD-132105. PubMed PMID: 24413614.
17. Park SW, Kim JH, Mook-Jung I, Kim KW, Park WJ, Park KH, Kim JH. Intracellular amyloid beta alters the tight junction of retinal pigment epithelium in 5XFAD mice. *Neurobiol Aging*. 2014 Mar 15. pii: S0197-4580(14)00242-5. doi: 10.1016/j.neurobiolaging.2014.03.008. [Epub ahead of print] PubMed PMID: 24709310.
18. Cheung CY, Ong YT, Ikram MK, Ong SY, Li X, Hilal S, Catindig JA, Venketasubramanian N, Yap P, Seow D, Chen CP, Wong TY. Microvascular network alterations in the retina of patients with Alzheimer's disease. *Alzheimers Dement*. 2014 Mar;10(2):135-42. doi: 10.1016/j.jalz.2013.06.009. Epub 2014 Jan 15. PubMed PMID: 24439169.
19. Gharbiya M, Trebbastoni A, Parisi F, Manganiello S, Cruciani F, D'Antonio F, De Vico U, Imbriano L, Campanelli A, De Lena C. Choroidal Thinning as a New Finding in Alzheimer's Disease: Evidence from Enhanced Depth Imaging Spectral Domain Optical Coherence Tomography. *J Alzheimers Dis*. 2014 Feb 20. [Epub ahead of print] PubMed PMID: 24577467.
20. Hickam JB, Frayser R, Ross JC. A study of retinal venous blood oxygen saturation in human subjects by photographic means. *Circulation*. 1963;27:375-383.

21. Narasimha-Iyer, H., et al. Automatic identification of retinal arteries and veins from dual wavelength images using structural and functional features. 8, s.l.: Biomedical Engineering, 2007, Vol. 54.
22. F. C. Delori, F. J. Rogers, S. E. Bursell, and J. S. Parker, "A System for Non-Invasive Oximetry of Retinal Vessels," in Frontiers of Engineering in Health Care, 1982. Proceedings, Fourth Annual Conference of the I.E.E.E. Engineering in Medicine and Biology Society, A. R. Potvin and J. H. Potvin, Eds. (Institute of Electrical & Electronics Engineers, New York, 1982), p.296.
23. Delori FC. Noninvasive technique for oximetry of blood in retinal vessels. Appl Optics, 27:1113-25, 1988
24. Riva CE. Noninvasive measurement of oxygen tension in the optic nerve head. Curr Opin Ophthalmol. 1998 Apr;9(2):56-60. Review.
25. Beach JM, Schwenger KJ, Srinivas S, Kim D, Tiedeman JS (1999) Oximetry of retinal vessels by dual-wavelength imaging: calibration and influence of pigmentation. J Appl Physiol 86:748– 758
26. Tiedman JS, Kirk SE, Srinivas S, Beach JM (1998) Retinal oxygen consumption during hyperglycemia in patients with diabetes without retinopathy. Ophthalmology 105:1:31-3634
27. Schweitzer D, Hammer M, Kraft J, Thamm E, Königsdörffer E, Strobel J (1999)
vivo measurement of the oxygen saturation of retinal vessels in health
volunteers. IEEE Trans Biomed Eng -4664544 doi:10.1109/10.804573
28. Hardarson SH, Harris A, Karlsson RA, Halldorsson GH, Kagemann L,
Zoega GM, Eysteinnsson T, Benediktsson JA , Thorsteinsson A
Beach J, Stefansson E (2006) Automatic re
Sci -4715011 doi:10.1167/iovs.06-0039
29. Hardarson SH, Stefansson E (2012) Retinal oxygen saturation is altered in diabetic retinopathy. Br J Ophthalmol 96:560-563
30. Hammer M, Vilser W, Riemer T, Schweitzer D (2008) Retinal vessel oximetry-calibration, compensation for vessel diameter and fundus pigmentation, and reproducibility. J Biomed Opt 13:054015. doi:10.1117/1.2976032
31. Hammer M, Vilser W, Riemer T, Mandecka A, Schweitzer D, Kuhn U, Dawczynski J, Liemt F, Strobel J (2009) Diabetic patients with retinopathy show increased retinal venous oxygen saturation. Graefes Arch Clin Exp Ophthalmol 247:1025-1030 25.

32. Hammer M, Heller T, Jentsch S, Dawczynski J, Schweitzer D, Peters S, Schmidtke K, Muller U (2012) Retinal vessel oxygen saturation under flicker light stimulation in patients with nonproliferative diabetic retinopathy. *Invest Ophthalmol Vis Sci* 53:7:4063- 4068
33. Khoobehi B, Firn K, Thompson H, Reinoso M, Beach J. Retinal arterial and venous oxygen saturation is altered in diabetic patients. *Invest Ophthalmol Vis Sci*. 2013 Oct 29;54(10):7103-6. doi: 10.1167/iovs.13-12723. PubMed PMID: 24114546.
34. Harris A, Dinn RB, Kagemann L, et al. A review of methods for human retinal oximetry. *Ophthalmic Surg Lasers Imaging* 2003;34:152–64.
35. Khoobehi B, Eaton AM, Wafapoor H, Fournier P, Firn K, Peters M, Rodebeck E, Templet B. Determination of oxygen saturation of the optic nerve head and overlying artery and vein using a snapshot multi-spectral imaging system. *Proc. SPIE*. 8229, Optical Diagnostics and Sensing XII: Toward Point-of-Care Diagnostics; and Design and Performance Validation of Phantoms Used in Conjunction with Optical Measurement of Tissue IV, 822906. (February 01, 2012) doi:10.1117/12.910030
36. Khoobehi B, Beach JM, Kawano H. Hyperspectral imaging for measurement of oxygen saturation in the optic nerve head. *Invest Ophthalmol Vis Sci*. 2004 May;45(5):1464-72. PubMed PMID: 15111603.
37. Lambrou GN, Greve EL. *Ocular Blood Flow in Glaucoma: Means, Methods and Measurements*. Kugler Publications, 1989. ISBN: 9789062990535

BIOGRAPHY

Kim Firn grew up in Rose Valley, Pennsylvania and attended Strath Haven High School. She earned a Bachelor's degree in neuroscience from Tulane University in May 2013. During her semester abroad at the University of Sydney, she assisted Dr. Dario Protti researching retinal endocannabinoids. After earning her Master's degree in neuroscience from Tulane University in May 2014, she will return to Australia to continue research. She plans to apply to M.D./Ph.D. dual programs in the future.